

19  
480808

# Structure and Materials Aspects of the PRIME Flight Test Vehicle

---

31 DECEMBER 1965

---

*Prepared by* J. MELTZER, J. ROSSOFF, and J. I. SLAUGHTER

*Aerospace Corporation*

and

J. STERHARDT

*Martin Company*

*Prepared for* COMMANDER SPACE SYSTEMS DIVISION

AIR FORCE SYSTEMS COMMAND

LOS ANGELES AIR FORCE STATION

*Los Angeles, California*



EL SEGUNDO TECHNICAL OPERATIONS • AEROSPACE CORPORATION  
CONTRACT NO. AF 04(695)-669

STRUCTURE AND MATERIALS ASPECTS  
OF THE PRIME FLIGHT TEST VEHICLE

Prepared by  
J. Meltzer and J. Rossoff  
System Planning Division

J. I. Slaughter  
Laboratory Operations

and

J. Sterhardt  
Martin Company

El Segundo Technical Operations  
AEROSPACE CORPORATION  
El Segundo, California

Contract No. AF 04(695)-669


31 December 1965


Prepared for  
COMMANDER SPACE SYSTEMS DIVISION  
AIR FORCE SYSTEMS COMMAND  
LOS ANGELES AIR FORCE STATION  
Los Angeles, California

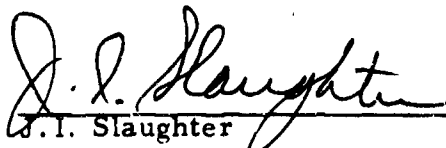
STRUCTURE AND MATERIALS ASPECTS  
OF THE PRIME FLIGHT TEST VEHICLE

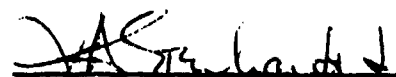
Prepared


Approved

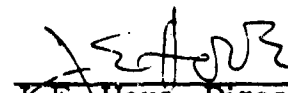
  
J. Meltzer  
System Planning Division

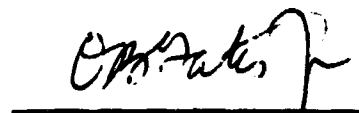
  
J. Rossoff  
System Planning Division

  
J. I. Slaughter  
Laboratory Operations


  
J. Sterhardt  
Martin Company, Baltimore

  
D. A. Rains, Associate Group Director  
General and Vehicle Planning  
Group Directorate  
System Planning Division

  
J. E. Hove, Director  
Materials Sciences Laboratory  
Laboratory Operations

  
O. B. Gates  
PRIME Technical Director  
Martin Company, Baltimore

This technical documentary report has been reviewed and is approved.

  
C. L. Scoville  
Colonel, USAF  
Director, Program START  
Research and Technology Directorate

## FOREWORD

This report was originally prepared as a preprint for the American Institute of Aeronautics and Astronautics / American Society of Mechanical Engineers Seventh Structures and Materials Conference to be held at Cocoa Beach, Florida, on 18 - 20 April 1966. The report is identical in content to the original paper.

Martin Company work reported herein was done under Contract AF 04(695)-643.

## ABSTRACT

The structure and thermal protection system being developed for the Air Force by the Martin Company as part of the START Program is described. The program is concerned with the design and flight test of a small maneuverable lifting reentry vehicle of the SV-5 configuration (hypersonic lift-to-drag ratio of approximately 1.3) with an ablative heat shield. Reentry conditions will simulate those encountered in return from low earth orbit. This program is expected to produce technology that could be applicable to manned, maneuverable reentry. A description of the thermal/structural configuration, load paths, materials used, discontinuities, and attachment to the launch vehicle is given. The influence of primary structural material on heat shield integrity and vehicle weight is discussed. Loading conditions and vehicle thermal/structural design criteria are described. The reentry environment of the vehicle is compared with related systems. Heating rates, total heats, shear loads, and pressures are shown, and thermochemical and thermophysical properties of various heat shield materials are discussed. Materials tests and data are compared with many applicable heat shield materials.

## CONTENTS

1.	INTRODUCTION . . . . .	1
2.	VEHICLE STRUCTURE . . . . .	5
2.1	Structural Description . . . . .	5
2.1.1	Structural Configuration . . . . .	5
2.1.2	Primary Structural Load Paths . . . . .	9
2.1.3	Equipment Access . . . . .	10
2.2	Reentry Vehicle/Launch Vehicle Attachment . . . . .	11
2.2.1	Structural Attachment . . . . .	11
2.2.2	Stiffness Requirements and Dynamic Effects . . .	12
2.2.3	Shroud Effects . . . . .	14
2.3	Loads, Criteria, and Environment . . . . .	15
2.3.1	Launch Conditions . . . . .	15
2.3.2	Reentry Conditions . . . . .	15
2.3.3	Recovery Conditions . . . . .	15
2.3.4	Structural Design Criteria . . . . .	17
2.3.5	Shock Environments . . . . .	21
2.3.6	Vibration Environments . . . . .	23
2.4	Stress Analysis . . . . .	26
2.4.1	Analysis Method Description . . . . .	26
2.4.2	Analysis Method Requirements . . . . .	28
2.4.3	Design Considerations . . . . .	30
2.5	Testing . . . . .	31
2.5.1	Development . . . . .	31
2.5.2	Verification . . . . .	31
3.	VEHICLE HEAT SHIELD . . . . .	47
3.1	Configuration and Materials Selection . . . . .	47
3.1.1	Comparison of Significant Flight Parameters for Typical Reentry Systems . . . . .	47
3.1.2	Summary of Reentry Environment, Materials Selection, and Program Objectives . . . . .	48

## CONTENTS (Continued)

3.1.3	PRIME Flight Test Plan and Reentry Environment . . . . .	49
3.2	Ablation Materials Selection . . . . .	50
3.2.1	Nose Cap and Flap Materials Testing and Selection . . . . .	50
3.2.2	Body Heat Shield Materials Testing and Evaluation . . . . .	53
3.2.3	Mechanical Properties of ESA-3560HF . . . . .	59
3.3	Thermal/Structural Design . . . . .	60
3.3.1	Heat Shield Design Factors . . . . .	60
3.3.2	Nose Cap Construction Details and Testing . . . . .	61
3.3.3	Body Heat Shield . . . . .	63
3.3.4	Fin and Antenna Window Heat Shield . . . . .	64
3.3.5	Flap Heat Shield . . . . .	65
REFERENCES . . . . .		R-1

## FIGURES

1.	Artist's Sketch of SV-5 Configuration . . . . .	3
2.	SV-5 Test Vehicle Inboard Profile . . . . .	3
3.	Structural Configuration . . . . .	33
4.	PRIME Nose Section . . . . .	33
5.	Recovery Hatch Cutting Action (Five-Grain) . . . . .	34
6.	Structure - Aft Body . . . . .	34
7.	Fin Structure . . . . .	35
8.	Flap Structure . . . . .	35
9.	Flap and Bearing Installation . . . . .	36
10.	Reentry Vehicle General Arrangement . . . . .	36
11.	Volume Utilization . . . . .	37
12.	Load Action of Structural Ball Joints . . . . .	37
13.	Post-Launch Oscillation Condition . . . . .	38
14.	BECO Transient Support Point Reactions . . . . .	38
15.	Launch Fairing Configuration . . . . .	39
16.	Launch Fairing Temperatures . . . . .	39
17.	Maximum Body Surface Distributions (Limit) . . . . .	40
18.	Reentry Vehicle Envelope Limit Bending Moments . . . . .	40
19.	Design Limit Recovery Loads (Parachute Deployment and Air Recovery Pickup) . . . . .	41
20.	Recovery Loads Application Variation . . . . .	41
21.	Comparison of Shock Response Spectrum Shapes for Test and Actual Pyrotechnic Environment . . . . .	42
22.	95 Percent PSD (Boost Environment) . . . . .	42
23.	Comparison of Measured Atlas Interface Vibration Data with Predicted Levels . . . . .	43
24.	95 Percent PSD (Reentry Environment) . . . . .	43
25.	Automatic Plotting Techniques . . . . .	44
26.	Typical Trimetric Plot (Structural Model) . . . . .	44
27.	Payload-Booster Interface . . . . .	45
28.	Dynamic Simulation . . . . .	45



# FIGURES (Continued)

29.	Typical Local Heating Rate Ratio . . . . .	67
30.	Typical Shears and Heating Rates for Nose Cap, Flap, Top, and Bottom of PRIME Vehicle . . . . .	67
31.	Typical Heat Balance for Low Density Ablator Plasma Arc Test at Moderate Heat Flux Showing Low Net Input to Substructure . . . . .	68
32.	Weight Comparison of Low Density Ablators with Standard Ablators for Typical Lifting Body Orbital Reentry Conditions (400°F Backface Temperature) . . . . .	68
33.	Typical Density Distribution for ESA-3560H Through Char and Pyrolysis Zones . . . . .	69
34.	Recession Characteristics of Low Density Ablators (32 lb/cu ft) . . . . .	69
35.	Insulation Efficiency of NASA/Langley Purple Blend with Fiber Addition . . . . .	70
36.	Improved Char Reinforcement by Glass Fiber Addition to ESA-3560HF . . . . .	70
37.	Ultimate Strain for Various Materials . . . . .	71
38.	Thermal Strain Failure Parameter versus Temperature . . . . .	71
39.	Carbon-Phenolic Nose Cap After Heat Test . . . . .	72
40.	Body Heat Shield Details . . . . .	72
41.	Bond Strength of HT-424 and EPON 934 Adhesives for Bonding E-Glass to Stainless Steel and Aluminum . . . . .	73
42.	Fin and Antenna Window Details . . . . .	73
43.	Flap Heat Shield Details . . . . .	74

## TABLES

1.	Design Limit Load Factors for PRIME Vehicle . . . . .	16
2.	Shock Sources . . . . .	22
3.	Structural Verification Testing Summary (Vehicle 1) . . . . .	32
4.	Structural Verification Testing Summary (Vehicle 2) . . . . .	32
5.	Design Limit Load Factors for PRIME Vehicle . . . . .	62

## 1. INTRODUCTION

The Air Force Space Systems Division is engaged in a program to flight test a maneuverable lifting body reentry vehicle (R/V) as part of the START Program. That portion of START, identified as Project PRIME (Precision Recovery Including Maneuvering Entry), is a four-flight hypersonic test program that will simulate low earth orbit reentry conditions of a small maneuverable test vehicle having precision recovery capability. This vehicle, the SV-5, has a hypersonic lift/drag (L/D) ratio of approximately 1.3. It is approximately 80 in. long and weighs approximately 900 lb. The SV-5 is being designed and built by the Martin Company, Baltimore, and is shown in Fig. 1. A schematic inboard profile is shown in Fig. 2.

The SV-5 will be launched by a General Dynamics/Convair SLV-3 booster.

Recent advances in ablation analyses, materials formulation, and manufacturing methods leading to a new class of low density ablative materials have been coupled with the development of compatible manned and unmanned lifting reentry configurations that permit maneuvering reentry and controlled landing at a selected land base. These vehicles are potentially reusable with minimum refurbishment and are economical, reliable, and have growth potential in payload capability and size. Extensive Air Force and NASA aerodynamic wind tunnel configuration studies have demonstrated that lifting body vehicles such as the SV-5 are capable of demonstrating the flight requirements of the PRIME Project. These shapes are simpler and have better volumetric efficiency than the higher L/D shapes of the  $L/D = 3$  class. Moreover, a subsonic L/D ratio of 4.5, well within the range of piloted capability for horizontal landing, may be achieved. Concurrently, Air Force sponsored programs have demonstrated that the low density ablation materials are simpler to process, more reliable, permit greater mission flexibility, and will take a higher heat flux overshoot without catastrophic failure as compared with state-of-the-art coated refractory metals.

The structural body configuration of the PRIME vehicle is basically a conventional arrangement of aluminum skin, stringers, and frames covered with a low density silicon elastomer ablator. Higher temperature materials are used for the fins and flaps to allow the use of relatively thin heat shields so that the control surface thickness can be maintained within aerodynamic configuration limitations. The thermal protection of the flaps, as well as the nose cap and body leading edges, is a carbon-phenolic ablator, while the fins are protected by the same materials as the body. During launch, the entire vehicle is protected from aerodynamic forces and heating by a shroud; this minimizes launch loading conditions on the vehicle and prevents degradation of the heat shield during launch so that the design and post-flight analyses of the heat shield can be applied essentially to the reentry environment.

Principal factors which define the structural/thermal design of the vehicle are: (1) R/V stiffnesses to minimize coupling of vehicle motions with launch vehicle (L/V) vibrations; (2) dynamic and static loading conditions at the R/V-L/V interface; (3) reentry heating; and (4) recovery conditions.

A detailed description of the PRIME design has been given by O. B. Gates of the Martin Company (Ref. 1). A status report on the PRIME thermal protection system was prepared earlier in the program by J. Meltzer and J. I. Slaughter of Aerospace Corporation and D. V. Sallis of the Martin Company (Ref. 2).

This report presents a summary of the structural design and heat shield development and concepts used for the PRIME thermal protection system.



Fig. 1. Artist's Sketch of SV-5 Configuration

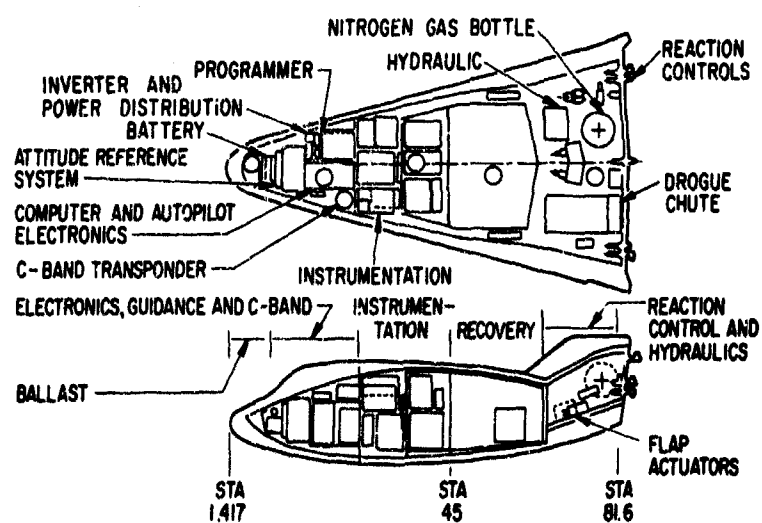


Fig. 2. SV-5 Test Vehicle Inboard Profile

## 2. VEHICLE STRUCTURE

### 2.1 STRUCTURAL DESCRIPTION

#### 2.1.1 Structural Configuration

Although the PRIME reentry vehicle is fabricated from five primary structural materials (excluding heat shield materials) ranging from beryllium to stainless steel and standard aluminum, the criterion for vehicle construction has been simplicity of fabrication within existing manufacturing technology. As a result, the basic R/V structure is 2014-T6 aluminum with a maximum expected temperature exposure to 300°F. The design allows for a 100°F overshoot. Almost no expenditures have been necessary for fabrication development of the vehicle structure.

Studies were made to determine the feasibility of working the body structure to 800°F which is approximately the pyrolysis level of the ablative heat shield. Considering structural efficiency and program costs, the most reasonable selection of a structural material for this case would be titanium. The titanium structure would be heavier than aluminum because of steeper thermal gradients on titanium, the lower buckling efficiency of titanium, and increased environmental control provisions for a titanium vehicle. However, the heat shield for a titanium vehicle would weigh less due to the allowance for a higher backface temperature. The net effect of these considerations showed that the titanium vehicle would be approximately 2 percent lighter than the aluminum vehicle. To gain this advantage, the shield thickness criteria for both cases would have to be the same. Consequently, the titanium vehicle at its maximum temperature would have a heat shield that was totally degraded, whereas the aluminum vehicle at its maximum temperature would have a portion of uncharred ablator adjacent to the structural body. Such a condition indicates a higher risk program and an inherently lower margin of safety with titanium. In addition, the increased development and more complex fabrication procedures that would be required for a titanium vehicle would cause an

appreciable increase in program costs. Therefore, the small potential weight advantage that could be obtained with an 800°F structure was rejected.

As shown in Fig. 3, the basic body structure comprises a forward removable "glove" section and a fixed aft structure. The forward glove is constructed generally of 0.060-gauge 2014-T6 skin, machined frames, and stringers. Both the frames and the stringers are continuous with the outstanding leg of the stringers cut out at each frame and the skin flange continuous under the frame. Frame spacing is approximately 11 in. with a maximum stringer spacing of 6 in. The glove is attached to the aft section by fourteen 1/4-in. tension bolts at station 45. When the glove is removed, the major equipment components, located on the vehicle equipment beam, are exposed for maintenance, servicing, and checkout.

The all-ablative heat shield is bonded directly to the outside skin and protects the structure to a maximum expected temperature of 300°F. The vehicle ablative nose cap and ballast are attached to the glove section at approximately station 12. The arrangement (shown in Fig. 4) provides for independent attachment of both the ballast and the ablative cap to the frame. This feature was incorporated to minimize load stresses into the all-ablative nose cap, to permit easy removal of the nose cap, and to facilitate variable ballast provisions.

The forward upper fairing (shown in Fig. 10) was provided to cover the forward main parachute attachment fitting. The removable fairing is constructed of reinforced glass fabric and the ablative heat shield is bonded directly to it. The main chute cable of 3/8-in. steel is located in a trough along the top centerline of the glove. The deploying action of the main chute forces the cable forward, and the cable (under load from the main chute) strips out the fiberglass fairing along perforations to expose the chute fitting. The cable attachment at frame station 21 then supports the vehicle during recovery operations.

The aft section of the vehicle contains all of the operating functional equipment and most of the complex body structure. Forward of the aft section, but attached to bulkhead 45, is the equipment beam.

The equipment beam, designed primarily for equipment support stiffness requirements, is constructed of 3/16-in. machined magnesium side plates to which most of the equipment is attached; 2014-T6 0.063-in. removable cover plates provide a closed section beam for torsional stiffness. The beam is cantilevered from and mechanically attached to bulkhead 45.

The aft section (from bulkhead 45 to the canted bulkhead) is 2014-T6 skin, stringer, and frame construction similar to the glove. It has a large structural hatch covering the entire upper surface between these two major bulkheads. The hatch is built up 2014-T6 sheet reinforced with beads to provide required panel stiffness and is attached to the body with equidistant 3/16-in. screws (see Fig. 3). The hatch support structure is comprised of machined flanges of bulkhead 45, the canted bulkhead, and two side coaming stringers. It provides for installation of a five-grain flexible linear shaped charge which cuts and blows off the recovery section hatch during recovery operations to permit deployment of the main chute from the compartment directly under the hatch. The cutting action of the charge is shown in Fig. 5.

The remaining section aft of the canted bulkhead is entirely machined, integrally stiffened 2014-T6 aluminum structure, including two upper structural access doors, a lower reinforced skin panel, a machined center beam, two side beams to which the fins are attached, and the aft bulkhead (Fig. 6). Each of the two lower flaps are attached to the aft structure by inboard and outboard Rene' 41 machined fittings and are operated by the hydraulic system control arms near the vehicle centerline. The R/V is attached to the SLV-3 launch vehicle at three locations on the aft bulkhead.

The aft bulkhead provides cutouts and support for the recovery system drogue chute container, three electrical connectors, two reaction control



system nozzle assemblies, an air inlet for the ground air cooling system, and exhaust nozzles for the airborne cold plate environmental control system. The aft body section is protected by the directly-bonded ablative heat shield.

The fins (Fig. 7) are composed of PH 15-7 Mo 3/8-in. steel honeycomb to which are bonded 0.040 and 0.020 in. beryllium faces. Beryllium was used in this application to take advantage of the large heat sink capability of this material which permitted a higher structural temperature (800°F) for the fin. The aerodynamic configuration dictated the fin thickness. The higher allowable structural temperatures permitted a much thinner heat shield and enabled the heat shield-structure composite to stay within the aerodynamic thickness limitations. Since fin load and flutter requirements were small enough to permit use of minimum gauges (see Section 2.3) and since the beryllium sheet panels could be flat with only a simple bend at the simulated rudder-fin intersection, the use of beryllium on the fins required only a minimal fabrication development program. Steel sheets could be used in the same application, but minimum gauge limitations would have resulted in a weight penalty, both in structure and added ballast.

The fins are mechanically attached to the body side beams by 1/4-in. bolts. Since the fins allow a higher structural temperature (800°F) than the body structure (400°F), the fins are attached to the body utilizing insulating spacers.

The flap structure also is allowed to reach 800°F. However, the flap temperature was established not only because of space limitations but also because structural heat shield studies determined that higher structural flap temperatures resulted in lower flap composite weight.

Beryllium (machined 1/2-in. stock) was used for the flap structure because of its high strength-to-weight ratio and specific heat (Fig. 8). The flap lower surface heat shield is both bonded and mechanically attached to the beryllium plate, while the upper surface heat shield is only bonded (see Section 3.2.1). The inboard and outboard Rene' 41 hinge fittings are bolted

to the beryllium flap plate. Rene' 41 spherical ball bearings coated with a gold plate lubricant (developed by Boeing under post-Dynasoar funding) are installed in the Rene' 41 fittings (Fig. 9).

Because of stiffness requirements to prevent cracking of the ablator and the high density of the vehicle, unit structural weights are somewhat above the normally used weight estimation averages. For example, the total body structure, including equipment supports and the equipment beam, weighs about 125 lb; with about 43 sq ft of wetted structural area, the basic structure weighs approximately 3 psf. The flaps weigh 17.4 lb (total) and the fins weigh 6.6 lb (total) for a gross structural weight of 149 lb.

For comparison, the basic body heat shield, including inserts and edge members, weighs approximately 161 lb. The external wetted area is 43 sq ft and the unit heat shield weight is 3.75 psf. The nose cap weighs 30 lb (excluding ballast), the fin heat shield weighs 11 lb, and the flap heat shield weighs 40 lb, for a gross heat shield weight of 242 lb.

Therefore, the composite structure and heat shield weighs 391 lb or 44 percent of the total vehicle gross weight of 890 lb.

#### **2.1.2 Primary Structural Load Paths**

As described in Section 2.3, the primary loadings on the R/V occur during launch (from booster induced accelerations), from the flaps during reentry maneuvering, from concentrated loads during the recovery operation sequence, and from thermally induced stresses. Body reentry aerodynamic loadings are generally small and only locally influence the design of the structure.

All doors and hatches are structural because of stiffness requirements during launch and because of the desire to provide minimum structural deflections for the structure that supports the heat shield. The structure is, therefore, essentially continuous. Launch loads result from booster induced accelerations. Since the R/V is protected by a fairing during launch, ascent

aerodynamic loads on the R/V do not exist. The launch loads enter the R/V structure as inertia loadings, build up axial and lateral loads and bending moments according to the R/V mass distribution, and lag out to the three aft booster attachment tension bolt fittings; lag is through the upper and lower skins, the side beams, and the center beam. The aft bulkhead redistributes shears and kick loads.

Flap loads are reacted by the inboard and outboard Rene' 41 fittings and flap actuator arm.

Concentrated loads occur during recovery. Drogue chute loads occur initially with the drogue attached to the aft bulkhead at the centerline. Loads are reacted by the center beam and are lagged to the upper and lower skins and forward to be reacted by aerodynamic and inertia body loadings.

When the main chute is deployed and the main recovery hatch is ejected, the local structure becomes discontinuous. Initial main chute loads are reacted by the two main chute bridle attachments at bulkhead 45 and at the main attachment fitting at station 21. After the initial vehicle motion has settled, the attachments at bulkhead 45 are cut, and vehicle support is solely at station 21. Loads entering at station 21 are distributed into the glove by the frame and upper fitting-stringer. Skin loads are lagged around the large recovery hatch cutout. Loads entering the station 45 bulkhead are sheared into the skin from the bulkhead.

### 2.1.3 Equipment Access

Most of the R/V operating equipment is located on the equipment beam forward of bulkhead 45. Access to this equipment is accomplished by removal of the forward glove and, as required, the upper cover plate on the equipment beam. To provide as favorable a ballast situation as possible, the equipment is located on the beam almost exclusively as a function of its weight or packaging density. Although the vehicle volume center is located at 57 percent of the aerodynamic length (which is actually forward of the desired 59 percent center of gravity (CG) requirement for aerodynamic stability), the

large volume of heat shield and structure aft of the desired CG requires almost 90 lb of ballast in the nose. Therefore, equipment is packaged as densely and as far forward as possible to offset the aft CG effect of the structure and heat shield. A general arrangement of the R/V is shown in Fig. 10.

Although several concepts of access were considered, including upper and lower access doors in the forward portion of the vehicle, it became evident that the sliding glove arrangement permitted a tighter and more dense packaging arrangement than any other method and at the same time provided the best access. As a result, equipment has been packaged in the R/V at better than  $35.5 \text{ lb/ft}^3$  and at a volume utilization of about 62 percent (Fig. 11). Of the 50 major components in the R/V, all but 4 can be removed without removing another.

Access to the main recovery components is accomplished by removing the main recovery hatch and then unbolting and disconnecting the main recovery container. The main recovery container is a five-sided box which contains the main parachute, water flotation system, and all the recovery operating components with the exception of the drogue system.

Two upper structural doors provide access to the equipment located in the aft compartment between the canted and aft bulkheads. All protruding items on the aft bulkhead may be removed without removing or damaging the heat shield.

## 2.2 REENTRY VEHICLE/LAUNCH VEHICLE ATTACHMENT

### 2.2.1 Structural Attachment

The R/V attachment to the L/V is accomplished through three tension attachment bolts at the R/V aft bulkhead. A typical attachment bolt fitting interface is shown in Fig. 12.

In order to provide for zero (or minimum) fixity at each of the three attachment points, the fittings were designed as ball joints and in such a manner so as to prevent or minimize bolt bending. The high strength (150,000 psi heat

treat) 5/8-in. steel bolts are threaded into the R/V ball fitting with the bolt head located in the booster interstage on a spherical washer (Fig. 12). The R/V ball portion is constructed of molded glass phenolic to protect the structure under the joint during reentry heating.

The 5/8-in. steel bolts are internal explosive bolts which detonate and fracture at R/V-booster separation. The bolt fracture occurs just aft of the R/V ball and leaves a portion of the bolt with the R/V after separation. An example of the load action of this joint is also shown in Fig. 12.

Since an explosive bolt induces a significant shock impulse, a shock absorbing mechanism was provided behind the bolt to take up the driving energy of the bolt following detonation. The bolt separates, slides forward (under the impulse of the explosion) in the sliding nut, and crushes a honeycomb shock absorber located behind the nut.

The entire ball fitting and assembly can be removed from the R/V bulkhead. During R/V transportation, the fittings are removed and replaced with a steel ball assembly to minimize damage to the threads in the flight ball fitting.

#### 2.2.2 Stiffness Requirements and Dynamic Effects

Although attachment of the R/V to the booster at the R/V aft bulkhead has many advantages, it provides a generally flexible interface. The basic R/V pitch frequency, cantilevered from an infinitely stiff restraint, is approximately 12 cps. Considering the local booster flexibilities or compliances, the R/V pitch frequency drops to 8.7 cps. The dynamic analysis derived by Kaufman-Hall (Ref. 3) was utilized to define and provide the proper R/V stiffness and booster support compliances necessary to minimize acceleration magnification factors during booster transient loading conditions. (The analysis method is described in Section 2.4.)

An example of the importance and significance of the R/V-booster compliance stiffness is illustrated in Fig. 13. The resultant R/V lateral load factor is plotted versus the natural frequency of the R/V when constrained by the

compliant support structure. The boost condition represented is post-launch oscillation which occurs immediately after launch and lasts for approximately 20 sec. At this time, the booster forcing frequency is 6 cps. Both transient and transient plus steady-state load factors are shown. The figure shows that as the R/V frequency approaches 6.5 cps, the resultant lateral load factor increases rapidly; below 6.5 cps, this factor becomes the designing launch condition.

The first analysis of proposed booster support structure compliances resulted in an R/V frequency of less than 7 cps. Considering analysis and construction uncertainties, it was determined that at least a 10 percent margin on frequency (or approximately 7.5 cps from the Kaufman-Hall element analysis) would be required to ensure at least 6.7 cps in the flight vehicle after assembly. Several iterations in the R/V structural sizes and booster compliances resulted in an R/V natural pitch frequency of about 8.7 cps, well out of the critical range.

Another acceleration transient occurs during booster engine cutoff (BECO). This transient is described as either a modulated sinewave having a peak transverse acceleration of 3.5 g or a peak torsional acceleration of 37.5 rad/sec<sup>2</sup>. The booster contractor defines this transient load condition in the lateral direction as

$$\ddot{Y} = 3.5 \sin(8\pi)t \sin(2\pi f)t$$

which contains the product of a 4 cps and a 50-80 cps sinusoidal load. This transient condition exists for approximately 1/2 cycle of the lower frequency sinusoid or 1/8 sec.

Figure 14 illustrates the effect of this transient load condition on the attachment reactions as a function of the booster forcing function frequencies between 54 and 81 cps. The R/V fourth, fifth, and sixth lateral frequencies are 58.5, 63, and 77 cps, respectively - well within the booster forcing

frequency range. The plotted reactions include the effects of steady-state load factors.

### 2.2.3 Shroud Effects

During boost ascent, the R/V is completely enclosed by a shroud or fairing (Fig. 15) to protect it from ascent aerodynamic loads, pressures, heating, and acoustic levels. The fairing separates at a dynamic pressure of about 5 psf, and as a result, the R/V is essentially unaffected by ascent aerodynamics and direct ascent heating. However, the fairing structural temperature rises significantly due to the ascent heating and, as a result, the fairing radiates to the R/V.

The unpainted R/V heat shield emissivity in the infrared range is approximately 0.90, and therefore the R/V heat shield absorbs a large percentage of this radiant heat flux. Since the heat flux is radiant and not convective, the temperature increase on the heat shield backface would be significant enough (15-25°F) to require either of two alternative actions: (1) insulate the inner wall of the shroud to prevent the radiation; or (2) paint the R/V heat shield with a metallized paint having an infrared emissivity near 0.3 and reflect the heat back to the shroud.

Figure 16 illustrates one shroud station cut and shows the temperature history of the inner and outer walls of the shroud and an insulation blanket inner surface temperature as a function of launch time. The insulating blanket weighs approximately 35 lb, and its effects are shown in Fig. 17. This blanket provides a suitable inner surface temperature history.

An R/V heat shield aluminized paint with an infrared emissivity near 0.3 is now being evaluated for effects on the ablative heat shield during reentry heating; no adverse effects are expected. The decision on whether to use the shroud blanket or the R/V paint will be made at the conclusion of these tests.

## 2.3 LOADS, CRITERIA, AND ENVIRONMENT

### 2.3.1 Launch Conditions

A summary of launch loading conditions is given in Table 1. Except for the BECO 70 cps transient dynamic loads, the launch conditions are represented in the table as load factors at the vehicle CG. At all the conditions shown except the BECO case, the R/V dynamics are not critical for design.

The importance of R/V dynamics in the BECO case is due to the extreme asymmetry of the R/V, the significant coupling between all three axes, and the critical nature of these loads. The dynamic loads of this case are best described for vehicle design as an acceleration time history at the R/V-booster interface, as shown in Table 1.

In addition to the BECO 70 cps transient condition, the maximum dynamic pressure and the post-launch oscillation conditions are critical during launch. Vehicle stiffness and separation fitting strength are the principal areas of structural design affected by launch loadings.

### 2.3.2 Reentry Conditions

As is characteristic of most lifting body vehicles, the reentry aerodynamic loads do not design any of the vehicle body structure. An example of the maximum body surface limit pressure distributions is shown in Fig. 17.

### 2.3.3 Recovery Conditions

The recovery loads occurring from drogue chute deployment through main chute deployment and air pickup are major design load conditions for the R/V. Water impact occurs at such a low sinking speed (approximately 21 fps) that the basic structure is unaffected by the low impact pressures. The limit bending moment plots for the various critical recovery conditions are shown in Fig. 18.



Table 1. Design Limit Load Factors  
for PRIME Vehicle

Condition	Static		Dynamic			Design Limit Loads			
	Long.	Lat.	Env. Vib. <sup>a</sup>	Long.	Lat.	Max. Long.		Max. Lat.	
						Long.	Lat.	Long.	Lat.
Thrust buildup	+1.0	0	±0.5	±5.2	±0.5	1.0 ± 5.7	±0.5	1.0 ± 5.2	±1.0
Launch release Liftoff acceleration	+1.48	±0.1	±0.5	±2.6	±0.5	1.48 ± 3.1	±0.6	1.48 ± 2.6	±1.1
Autopilot activation	+1.48	±0.1	±0.5	±0.6	±1.0	1.48 ± 1.1	±1.1	1.48 ± 0.6	±1.6
Post-launch longi- tude oscillations	+1.6	±0.1	±0.5	±0.3	±0.5	1.6 ± 0.8	±0.6	1.6 ± 0.3	±1.1
Mach 1 to max q	2.5	±0.34	±0.5	0	±1.41	2.5 ± 0.5	±1.75	2.5	±2.25
Maximum <u>booster</u> acceleration	7.7	±0.1	±0.3	0	±0.1	7.7 ± 0.3	±0.2	7.7	±0.5
BECO 70 cps transient	3.0	±0.1	b	±1.0	b				
Maximum <u>sustainer</u> acceleration	9.3	±3.33	±0.1	0	±0.1	9.3 ± 0.1	±0.43	9.3	±0.53

<sup>a</sup> Lateral or longitudinal, but not both at same time

<sup>b</sup> Torsional and lateral input levels are as follows: conditions do not occur simultaneously. These are applied at the interface.

Condition I: (rotational acceleration in rad/sec/sec)

$$\ddot{\theta} = 37.5 \sin 8\pi t \sin 134\pi t, \text{ for } 0 \leq t \leq 1/8 \text{ sec;}$$

$$= 0 \text{ for } 0 \geq t \geq 1/8 \text{ sec}$$

Condition II: (translational acceleration in g's;  $\ddot{x}$  = pitch,  $\ddot{y}$  = yaw)

$$\text{Lateral } (\ddot{x} \text{ or } \ddot{y}) = 3.5 \sin 8\pi t \sin 134\pi t, \text{ for } 0 \leq t \leq 1/8 \text{ sec;}$$

$$= 0 \text{ for } 0 \geq t \geq 1/8 \text{ sec}$$

Three separate recovery conditions are critical (see Figs. 19 and 20):

- a. Drogue deployment and steady state loads, with the drogue force applied to the aft bulkhead. The variation of this load as a function of load application angle  $\phi$  is shown in Fig. 20. The load is maximum when  $\phi = 0$  deg or when the load passes through the R/V CG.
- b. Main chute initial deployment loads when the main chute first deploys with a bridle arrangement attached at bulkhead 45 and station 21. The critical load occurs when the bridle riser at bulkhead 45 is parallel with station 45.
- c. Air recovery pickup loads occur after the bridle has been separated from station 45 and the vehicle is hanging tail down from a single riser attached at station 21. The variation of this load with angular displacement is shown in Fig. 20. These loads are maximum when the recovery aircraft engages the main chute.

#### 2.3.4 Structural Design Criteria

In many cases the structural design criteria for this vehicle must be integrated and combined with the heat shield design criteria since the heat shield is bonded directly to the structure. The criteria, design, analysis, and fabrication of the structure and the heat shield must be considered as a composite in most cases. A summary of the basic criteria is given below.

##### 2.3.4.1 Basic Criteria

The load carrying structure for the body shell, fins, flaps, and rudders is a metal internal structure which is protected thermally with a nonstructural external ablative heat shield. This internal structure is designed to carry the critical loads and provide the required stiffness without the aid of the heat shield. However, any adverse effects of the stiffness contributed by the heat shield are considered; e.g., combined heat shield and structure frequency coinciding with boost vehicle frequencies.

The structural and thermal integrity of the heat shield is maintained during the entire mission through aerial recovery. There is no design requirement for retention of the heat shield during water recovery. Surface recession may occur, but material selection should minimize release of particulate matter from the surface.

The heat shield provides thermal protection for the internal structure by maintaining the structure temperatures at the design levels utilized in the strength and deflection analyses of the structure.

The internal structure provides a continuous support for the heat shield. For low density honeycomb reinforced heat shield materials, the primary attachment to the structure is through the honeycomb-to-structure bond. For the high density heat shield materials of the nose cap and flaps, the attachment to the structure is by mechanical means or by a combination of mechanical attachments and adhesive bonding. Similar requirements are considered for other areas that employ high density materials.

The strain of the heat shield due to structural loading, temperature gradients, dissimilar coefficients of expansion, and material curing processes is considered in the design of the heat shield.

In the structural design of the vehicle, the allowable stress or strain reflects the effects of the load, temperature, and time associated with the discrete and cumulative design environments. These include the reduction in strength and stiffness due to exposure to temperature and stress, plastic deformations due to applied stress, oxidation, and loss of ductility. Minimum guaranteed strength properties are used in the design of single load path structures. For multiple load path structures, 90 percent probability properties are used. Design mechanical properties are based on MIL-HDBK-5, references approved by government agencies, or as established by test.

The structure and heat shield are designed to sustain all recovery loads in combination with appropriate temperatures and with material properties as influenced by the prior phases of the mission.

#### **2.3.4.2 Structure Temperature Limits**

The maximum expected temperature of the body shell is 300°F; the maximum expected temperature for the lower flaps and fins is 700°F, based on calculations employing unfactored heating rates for critical dispersed trajectories. The design allows for a 100°F overshoot.

The recovery hatch shaped charge is not to exceed a temperature of 140°F below the maximum operational temperature of the shaped charge.

#### 2.3.4.3 Combination of Load and Thermal Effects

The R/V structure was analyzed for the combinations of load and temperature defined below.

<u>Condition</u>	<u>Temperature Used for Determining Allowable Strength</u>	<u>Temperature Gradient for Determining Thermal Stress</u>	<u>Structural Load</u>	<u>Allowable Strength</u>
A	Case I	Case I	Ultimate	Ultimate
B	Case I	Case I	Limit	Yield
C	Case I + 100°F	Case I + 100°F	Limit	Ultimate
D	Case II	Case II	Limit	Ultimate
E	Case III	Case III	Limit	Ultimate

Condition A - Structure shell temperatures were calculated from the dispersed design trajectory heating rates (Case I). The resulting thermal gradients were used for determining thermal stresses which, when combined with the appropriate time-dependent ultimate structure condition stresses, are not to exceed the ultimate strength of the structure at the above calculated temperatures.

Condition B - The thermal stresses of Condition A in combination with the time-dependent limit structure load stresses are not to exceed the yield strength of the structure at the above calculated temperatures.

Condition C - Structure shell temperatures were determined by adding 100°F to each structural element temperature from Condition A. The resulting thermal gradients were used for determining thermal stresses which, when combined with the appropriate time-dependent limit structural load stresses, are not to exceed the ultimate strength of the structure.

Conditions D and E - Structure shell temperatures were calculated from the dispersed trajectory heating rates that were modified by special temperature distribution to provide Cases II and III. The resulting thermal gradients were used for determining thermal stresses which, when combined with appropriate limit structural load stresses, are not to exceed the ultimate strength of the structure.

#### 2.3.4.4 Safety Factors

The following safety factors were applied to limit loads to obtain ultimate loads:

	<u>Ultimate</u>
Hazardous to personnel	1.50
Nonhazardous to personnel	1.25

The proof and burst factors for components mounted on or in the vehicle are as specified in the following tabulation. The factors were applied to the nominal operating pressures (e.g., 1500 or 3000 psi, etc.) under 1 g loading conditions. The design of all components included consideration of any loads that may result from transients, accelerations, and vibrations, and further included consideration of operating temperatures. The factors were multiplied (as applicable) by the appropriate preceding factors of safety.

<u>System</u>	<u>Factors</u>	
	<u>Proof</u>	<u>Burst</u>
Hydraulic system		
Lines and fittings	2.0	4.0
Accumulators	2.0	4.0
Actuators and other components subject to system pressure	1.5	2.5
Components subject to backpressure only (except lines and fittings)	1.5	2.5

<u>System</u>	<u>Factors</u>	
	<u>Proof</u>	<u>Burst</u>
Reaction control system		
Lines and fittings	2.0	4.0
Other components	1.5	2.5
Pressure vessels	2.0	2.5
(nominal operating pressure = 3000 psi maximum operating pressure = 3750 psi)		
Environmental control systems		
Lines and fittings	2.0	4.0
Other components	1.5	2.5
<u>Bolts and Fittings</u>		
Single bolt shear attachments		1.25
Single bolt tension attachments		1.15
All fittings		1.15

### 2.3.5 Shock Environments

There are nine specific events from launch through recovery which produce significant shock pulses to the R/V structure and its operating equipment. The events, the shock sources, the time of occurrence, and the equivalent half sine pulse shock definition are summarized in Table 2. Of the nine shock sources, booster separation and recovery hatch deployment are the most severe and produce the shock environment levels to which the vehicle components are qualified.

The shock absorbing mechanism located adjacent to the forward face of each explosive separation bolt is expected to reduce shock impulses in equipment components to an acceptable level (see Section 2.2.1).

The shock resulting from the five-grain flexible linear shaped charge used for recovery hatch removal is considered to be within qualification levels.

Table 2. Shock Sources

Time	Event	Device	Estimated Component Shock Response
T + 303	Jettison shroud	Douglas A-12 explosive fasteners on interstage ring	800 g at 0.2 ms (max); 60 g at 0.5 ms (min) at the R/V-L/V interface
T + 320	RCS activate	Squib valve (3.3 grain)	500 g at 0.2 ms half sine <sup>a</sup>
T + 321	Booster separation	3 high shear explosive bolts	800 g at 0.2 ms half sine; 3 concurrent shocks <sup>a</sup>
T + 1621	Drogue deploy	PC-24 cartridge	200 g at 0.4 ms half sine <sup>a</sup>
T + 1703	Hatch removal	FLSC 5-grain/ft	1850 g at 0.30 ms half sine <sup>a</sup>
T + 1703.5	Drogue release	PC-10 cartridge	1650 g at 0.25 ms half sine <sup>a</sup>
T + 1620 to T + 3300	Electrical switching from recovery sequencer	Pyrotechnic relay (<1/20 grain)	<1000 g at 0.2 ms; local only
T + 3300	Main chute release at water impact	Explosive cartridge	800 g at 0.2 ms half sine <sup>a</sup>
T + 3300	Flotation bag inflation	Squib valve (3.3 grain)	500 g at 0.2 ms half sine <sup>a</sup>

<sup>a</sup>The shock environment is generally defined here to be located approximately 1 ft from the source.

These levels are to be verified by the R/V verification test program described in Section 2.5).

An underlying consideration in evaluating the adequacy of the equipment for the pyrotechnic shock environment is the difficulty in simulating the shock environment. A comparison between the shock response spectra obtained with laboratory test equipment and the actual environment is shown in Fig. 21. Because of the relatively low shock response in the frequency range from 100 to 500 cps for the actual shock, laboratory tests must be ultra-conservative to ensure equipment adequacy over the entire frequency range. With the five-grain flexible linear shaped charge, it is expected that the test shock spectrum will not be exceeded except at the very high frequencies and that it will provide reasonable margins.

#### 2.3.6 Vibration Environments

Because of the similarity in type of mounting and location in the booster, Titan I truss data were used as a reference to predict the SV-5 vibration environment during the boost phase. Statistical analyses have been performed on the available Titan data, and the Titan 95 percent power spectral density (PSD) probability levels were used to predict a 95 percent PSD probability level for the SV-5.

Since the vibration is primarily acoustically induced, the base data were corrected on the basis of the acoustic pressure and dynamic pressure differences which exist between the Atlas/SV-5 configuration and the Titan I configuration. The data were then corrected for weight differences between the two configurations. However, no attempt was made to change the spectral distribution of response.

For the launch case, the following extrapolation method was used to predict the SV-5 acceleration spectral density:

$$G_{SV-5} = G_{T-I} \left( \frac{P_{SLV-3}}{P_{T-I}} \right)^2 \left( \frac{W_{T-I}}{W_{SV-5}} \right)$$



where

$G_{T-I}$  = 95 percent PSD of the Titan I truss during the first stage stacked captive firing in 50 cps bands from 20 to 2000 cps

$W_{T-I}$  = total weight of the Titan I truss with mounted equipments

$W_{SV-5}$  = total weight of the SV-5 vehicle

$P_{SLV-3}$  = sound pressure level in octave bands outside the SV-5 support truss (calculated by the methods of Kaufman-Hall) using the various SLV-3 engine parameters

$P_{T-I}$  = sound pressure level in octave bands outside the Titan I truss (calculated by the methods of Kaufman-Hall) using the various Titan I engine parameters

The transonic and maximum dynamic pressure predictions were analyzed in the same manner. The extrapolation equation used was:

$$G_{SV-5} = G_{T-I} \left( \frac{q_{SLV-3}}{q_{T-I}} \right)^2 \left( \frac{P/q_{SLV-3}}{P/q_{T-I}} \right)^2 \left( \frac{W_{T-I}}{W_{SV-5}} \right)$$

where

$G_{T-I}$  = 95 percent PSD of the Titan I truss during the transonic or max q periods of flight (whichever is applicable) in 50 cps bands from 20 to 2000 cps

$W_{T-I}$  = total weight of the Titan I truss with mounted equipments

$W_{SV-5}$  = total weight of the SV-5 vehicle

$q_{SLV-3}$  = free-stream dynamic pressure of the SLV-3 at either Mach 1 (735 psf) or max q (1025 psf), whichever is applicable

- $q_{T-I}$  = free-stream dynamic pressure of the Titan I at either Mach 1 (635 psf) or max q (765 psf)  
 $p/q_{SLV-3}$  = ratio for the SLV-3 of the root-mean-square fluctuating pressure in one-third octave bands to the free-stream dynamic pressure  
 $p/q_{T-I}$  = ratio for the Titan I of the root-mean-square fluctuating pressure in one-third octave bands to the free-stream dynamic pressure

The resulting acceleration spectral density is shown in Fig. 22.

Vibration environments measured on Atlas SLV-3 flights were recently obtained. The comparison with specified L/V interface levels is shown in Fig. 23. As can be seen, the vibration environment obtained by the above methods early in the program is conservative.

To predict a reentry vibration environment for the SV-5 equipment, the following extrapolation equation was used:

$$G_{SV-5} = G_{T-I} \left( \frac{P_{SV-5}}{P_{T-I}} \right)^2 \left( \frac{\sigma_{T-I}}{\sigma_{SV-5}} \right)^2 \left( \frac{W_{T-I}}{W_{SV-5}} \right)$$

where

- $G_{T-I}$  = 95 percent PSD of the Titan I truss during the second stage side-by-side captive firing  
 $\sigma_{T-I}$  = surface density of the Titan I structure (1.3 psf)  
 $\sigma_{SV-5}$  = ablated surface density of the SV-5 heat shield and skin (3.4 psf)  
 $W_{T-I}$  = total weight of the Titan I truss with mounted equipments (approximately 800 lb)  
 $W_{SV-5}$  = total weight of the SV-5 equipment truss with mounted equipments (approximately 185 lb)

$P_{T-I}$  = acoustic spectrum of the Titan I in one-third octave bands

$P_{SV-5}$  = acoustic spectrum of the SV-5 vehicle in one-third octave bands

The SV-5 acoustic spectrum was obtained by enveloping data from microphones on hypersonic "buzz" wind tunnel models and rescaling it to a maximum dynamic pressure of 440 psf. One of the microphones was flush-mounted with the underside of the vehicle forward of the flap and the other was flush-mounted with the vehicle base. The resulting vibration environment is shown in Fig. 24.

## 2.4 STRESS ANALYSIS

### 2.4.1 Analysis Method Description

The analysis of the R/V for both the launch and the free-flight condition was performed using an IBM 7094 computer program and based on the method formulated by Kaufman and Hall (Ref. 3). This method represents the structure in three dimensions by a number of discrete simple structural elements connecting together a grid pattern. The element arrangement used closely represents the actual geometric position of the major structural members (see Fig. 26). The structure is represented by a mathematical model using tension, torque, bending, and shear panel elements, and includes the elastic coupling between these elements. In this particular model the structure was represented with approximately 1800 elements of which approximately half were redundant. The mass properties of the vehicle were represented by a number of discrete masses having freedom to move in three orthogonal directions. A total of approximately 300 deg of freedom was used in a model. Separate models were used to evaluate the symmetric and antisymmetric loading and modes of the vehicle. In addition, the vehicle structure was partitioned into five major sections to facilitate the analysis: the glove, the equipment beam, the recovery section, the aft section from the canted bulkhead to the aft bulkhead, and the fins. For the boost condition, the vehicle model was supported by compliant reactions at the booster

attachment points. The structure was subsequently freed to determine the free-flight modes.

The digital program is designed such that element loads can be efficiently determined for numerous sets of critical loading conditions associated with launch through recovery. Static loads representing steady-state conditions and dynamic loads arising from the application of transient forces are thereby incorporated into the structural design. Dynamic loads in the structural elements are based upon the response in a sufficient number of three-dimensional vibration modes. The program also includes the capability to determine internal thermal stresses for prescribed temperature loadings.

In order to interpret the results obtained from the analysis, automatic plotting techniques were found to be necessary (Fig. 25). In the initial stages of model formulation, errors in locating the grid points were determined by trimetric plotting of the model such as shown in Figs. 25 and 26. Upon completion of the vibration analyses, the identification of the various vehicle modes was accomplished from automatic plots of the mode shapes as shown in the figure. The R/V boost configuration is inherently flexible due to a small vertical distance between the support points which react pitch bending moments. In addition, the pitch flexibility is largely influenced by the degree of structural continuity between the body's aft and midsections. It is difficult to use all of the load-carrying structure efficiently when providing load paths from the three interface support paths. A maximum stiffness design was required to meet established criteria for the avoidance of R/V frequencies in the range of booster excitation frequencies for particular coordinate directions. This design was affected by evaluating the strain energy contribution of each element to the total strain energy when applying unit acceleration load factors. Local flexibilities of the R/V support structure were considered in the frequency calculations since they have been found to affect fundamental rigidly supported structure frequencies by as much as 50 percent.

Since the booster contractor has the responsibility of providing quasi-steady load factors, a beam analogy of the three-dimensional model was constructed for incorporation in combined booster and R/V structural analyses (Fig. 27). The derivation of an analogous beam consists primarily of approximating beam stiffness distributions which result in fundamental modes nearly identical to those given by the three-dimensional model. A comparison is presented in Fig. 28 between the structural stiffness distribution obtained by classical "beam-type" analysis and that which is required to give the beam analogy similar modal properties. In addition to defining quasi-steady loads during the launch phase, the booster contractor also defined booster acceleration transients occurring at the interface. Corresponding element loads in the three-dimensional model were determined by force-response analyses and are used for verification of the structural design. A sufficient number of normal modes excited by the time-dependent boundary conditions are used to obtain total loadings in each element.

Aerodynamic and aeroelastic dependent problems (such as fin flutter, flap buzz, and flap control stability) that may arise during the reentry portion of flight were investigated by preliminary analyses and experimental test programs. Analyses of these problem areas were accomplished using the vibration modes and frequencies determined from the vehicle analysis. In addition, the cantilever modes of the fin were determined using the same digital program to determine camber deflections, and they were used in the flutter analysis.

It was concluded that accurate analysis of maneuverable R/V structures of the type described could not be accomplished without a three-dimensional mathematical model of the structure.

#### 2.4.2 Analysis Method Requirements

The complex SV-5 structural model was designed to handle the complete spectrum of mission requirements from liftoff through recovery. To analyze the vehicle with the accuracy required, it was necessary to represent the

structure in its entirety incorporating relatively greater detail in critical areas. Because of the size and complexity of the model, the composite structure was conceptually partitioned into five segments which could be treated individually and joined together at the segment interfaces. Wherever possible, manufacturing splices of major subassembly connections were used as the analytical boundaries of the structure. Within the segments, individual subsystems were isolated from the adjacent structure by specifying duplicate elements at the subsystem interfaces.

The external heat protection system was assumed to be nonstructural because of its low modulus of elasticity when compared to the aluminum structure. Therefore, the additional complexity required to incorporate the effect of the heat shield into the analytical model was not warranted.

The requirements of the SV-5 complex model are as follows:

a. Dynamics

- 1) Flexible support case - predict steady-state and transient responses for all conditions from prelaunch acceleration to sustainer engine cutoff
- 2) Rigid support condition - provide data for ground vibration survey
- 3) Free-free vehicle - furnish flutter and control stability data; predict drogue chute mortar pulse and drogue chute deployment responses
- 4) Free-free recovery vehicle (with recovery section hatch removed) - evaluate main chute deployment, air recovery, and water recovery loads

b. Booster-R/V Interface

- 1) Furnish model loads to evaluate support reactions at booster engine cutoff
- 2) Determine support reaction loads for steady-state ascent load factors
- 3) Supply influence coefficients at the support interface to evaluate the effects of vehicle deformation on interface components

c. **Stress-Strain Analysis**

- 1) Obtain stresses and strains due to inertia, air and thermal loads for the entire vehicle
- 2) Determine over-all loads for local panel buckling analysis
- 3) Determine contributions of individual structural components to over-all vehicle stiffness with regard to possible weight savings requirements

d. **Controls**

- 1) Determine structural environment of flap, actuator, and other frequency-sensitive control devices
- 2) Provide coupled fin-body frequencies and mode shapes for flutter and stability control analysis

2.4.3 **Design Considerations**

In its most efficient application, the Kaufman-Hall program would be used in the preliminary design of a vehicle structure. Critical load paths and elements which contribute most or least to the basic vehicle strength and stiffness could be defined. An iteration could then be performed to add or subtract strength, area, or stiffness where it would be most efficient from the standpoint of total vehicle weight.

On the PRIME vehicle a reasonable amount of this iteration was possible, especially to stiffen the R/V to obtain higher natural bending frequencies to alleviate the dynamic magnification factors present in the post-launch oscillation condition described in Section 2.2.2.

The structural elements (stringers, frames, skin panels, etc.) were ultimately defined in terms of area and gauges almost totally from local loads, thermal stress buckling criteria, stiffness requirements, and minimum gauges. Over-all bending was not a major contributor to structural member sizing. For example, the aft bulkhead, center beam, and side beam were designed from the local launch and drogue parachute loads. Glove

frames were critical for the ballast attachment and the main parachute loads at station 21. The equipment beam was designed to meet stiffness requirements.

Thermal stresses, however, did design nearly all the skin panels. Since the thermal stresses are a function of the temperature distribution resulting from the heat shield design and the final reentry heating trajectories, the calculation of the temperature gradients lags the requirement for establishing skin gauges and structure. Therefore, an extensive effort was initiated early in the program to estimate the effect of various possible temperature gradients on the structure thermal stresses. As a result of this study, panel buckling was established on the basis of 10,000 psi longitudinal thermal plus static stresses. Calculated maximum thermal stresses in the panels (near the end of heating and during the recovery phase) were of the order of 8000 psi, and maximum bending stresses at this time were less than 2000 psi.

## 2.5 TESTING

### 2.5.1 Development

In view of the generally conventional design and construction of the R/V, there was little need for development testing of the structure itself. A series of panel buckling tests was conducted at room and elevated temperatures. The panels represented typical curved sheet-stringer configurations and testing was conducted with and without a heat shield. One of the objectives of the tests was to determine the effect of a load-induced panel buckle on the char of a heated panel. The tests indicated that: (1) the char heat shield increased the panel buckling level by about 20 percent (although the design criteria do not allow the use of this extra capability); and (2) panel buckling during char formation does not create a catastrophic heat shield char fracture.

### 2.5.2 Verification

The major structural verification tests are to be conducted on two vehicles that are structurally identical to the flight vehicles. Vehicle 2 has a complete



heat shield, while vehicle 1 has none except for local simulation during a series of shock tests. Since the critical launch loads and vibrations occur while the vehicle has a complete and uncharred heat shield, these loads are conducted on vehicle 2 in order to assess any damage to the heat shield. Vehicle 1 is used to simulate the recovery loads and thermal stresses that occur late during reentry when the heat shield is charred and at the end of its useful life. Tables 3 and 4 summarize the tests to be conducted on these vehicles.

Table 3. Structural Verification Testing Summary (Vehicle 1)

Test Title	Description
1. Shock tests	1. Tests to establish shock levels throughout the R/V due to major shock sources: hatch, separation bolts, and drogue mortar.
2. Reentry and chute loads tests	2. Tests to simulate design temperature distribution with banks of quartz radiant lamps. Local reentry chute loads and fin and flap loads will be applied. Load and heat programmed as a function of time. Limit and ultimate loads.
3. Water drop and flotation	3. Vehicle to be dropped to produce design sinking speed at water impact. Water flotation system to be activated. Object is to verify flotation system operation during structural deformation.

Table 4. Structural Verification Testing Summary (Vehicle 2)

Test Title	Description
1. Ground resonance survey	1. Vehicle vibrated in various free-free and fixed mode conditions to establish vehicle natural frequencies and flap impedance.
2. Flight level random vibration	2. Structure subjected to flight level random vibration to verify structural integrity and define and minimize local equipment resonances.
3. Ascent loads	3. Axial, normal and lateral ultimate loads applied to structure to simulate critical ascent loads conditions at room temperature.
4. Handling and transportation	4. Ultimate local handling and transportation loads will be applied to fittings.

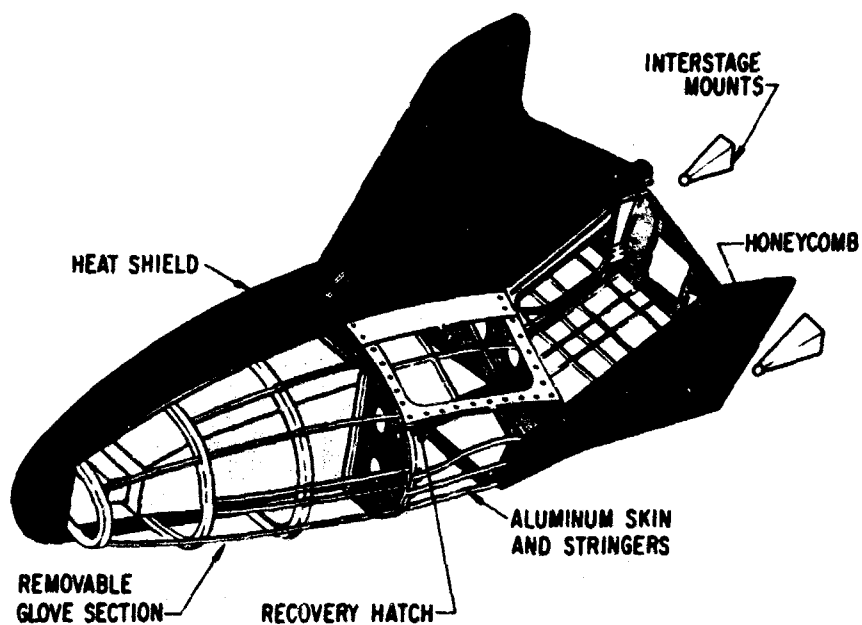


Fig. 3. Structural Configuration

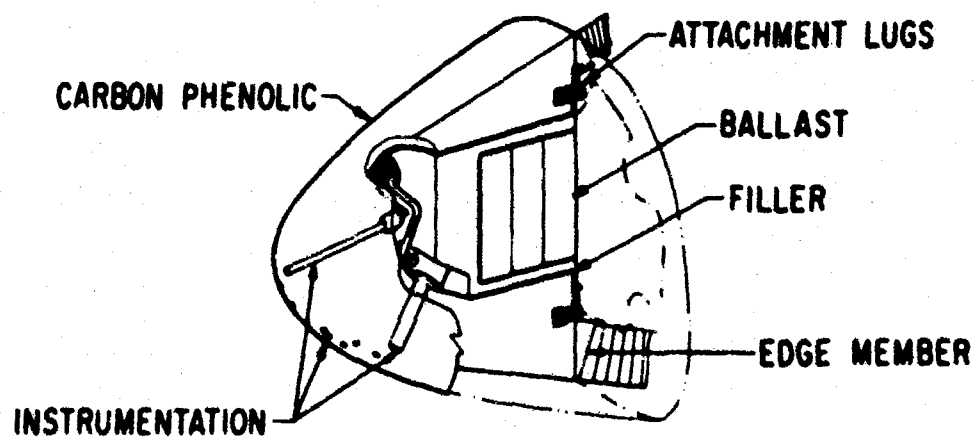
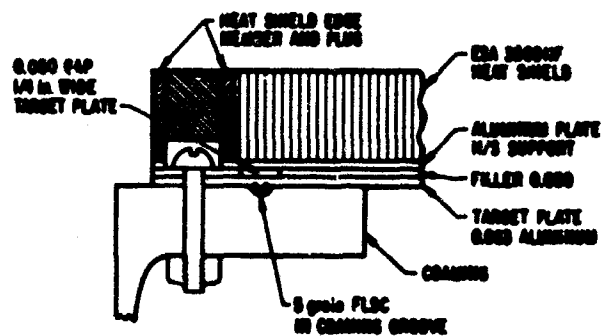
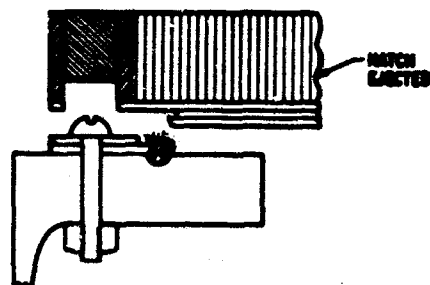


Fig. 4. PRIME Nose Section



**BEFORE INITIATION**



**AFTER INITIATION**

**Fig. 5. Recovery Hatch Cutting Action (Five-Grain)**

- **CONSTRUCTION**
  - RIVETED AND BOLTED ASSEMBLY
  - MACHINED BULKHEAD FRAMES AND FITS
  - INTERNALLY STIFFENED MACHINED SIDE PANELS BETWEEN CANTED AND AFT BULKHEADS
  - EXTRUDED STRINGERS
  - T-JOIN HAMMER FORMED SKIN, STR 45 TO CANTED BULKHEAD
- **MATERIALS**
  - 2014-T6 BARE SHEET, PLATE AND EXTRUSION
- **CRITICAL ENVIRONMENT**
  - ASCENT LOADS
  - RE-ENTRY THERMAL STRESS
  - DROGUE AND MAIN CHUTE RECOVERY LOADS
  - LOCAL HANDLING LOAD
  - 2 ps (LIGHT) PRESSURE DIFFERENTIAL
  - FLAP LOADS
  - PYROTECHNIC SHOCK

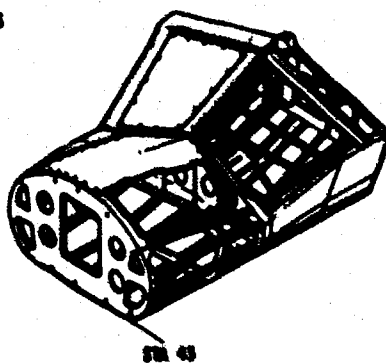
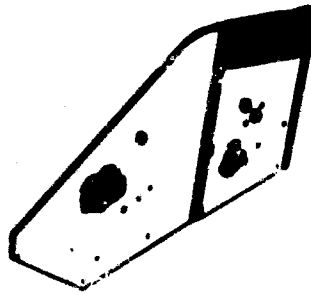


**Fig. 6. Structure - Aft Body**



● CONSTRUCTION

- BONDED HONEYCOMB SANDWICH

● CRITICAL CONDITION

- RE-ENTRY THERMAL STRESS

● MATERIALS

- CROSS ROLLED B<sub>2</sub> SHEET FACES
- 15-7 PH STEEL HONEYCOMB CORE
- HOT PRESSED B<sub>2</sub> BLOCK ANTENNA AND LEADING EDGE
- 15-7 PH STEEL SHEET TRAILING EDGE
- HT 424 ADHESIVE

Fig. 7. Fin Structure



● CONSTRUCTION

- BOLTED ASSEMBLY
- MACHINE FORGED PLATE
- MACHINE HINGE FITTINGS

● CRITICAL CONDITION

- OUTPUT OF ACTUATOR AT 1500 PSI (1535 PSI LIMIT) WITH B<sub>2</sub> AND REINE FITTINGS AT 800°F

● MATERIALS

- FORGED B<sub>2</sub> PLATE
- REINE 41 HINGE FITTINGS
- REINE 41 BEARINGS WITH HIGH-TEMP LUBE
- HEAT SHIELD-ABLATIVE (NOT SHOWN)

Fig. 8. Flap Structure

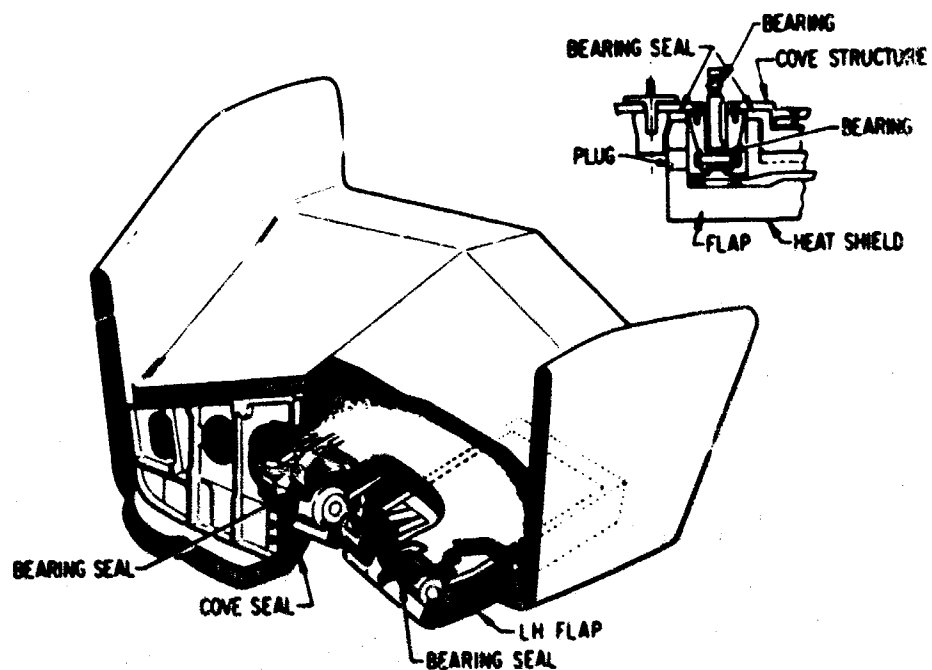


Fig. 9. Flap and Bearing Installation

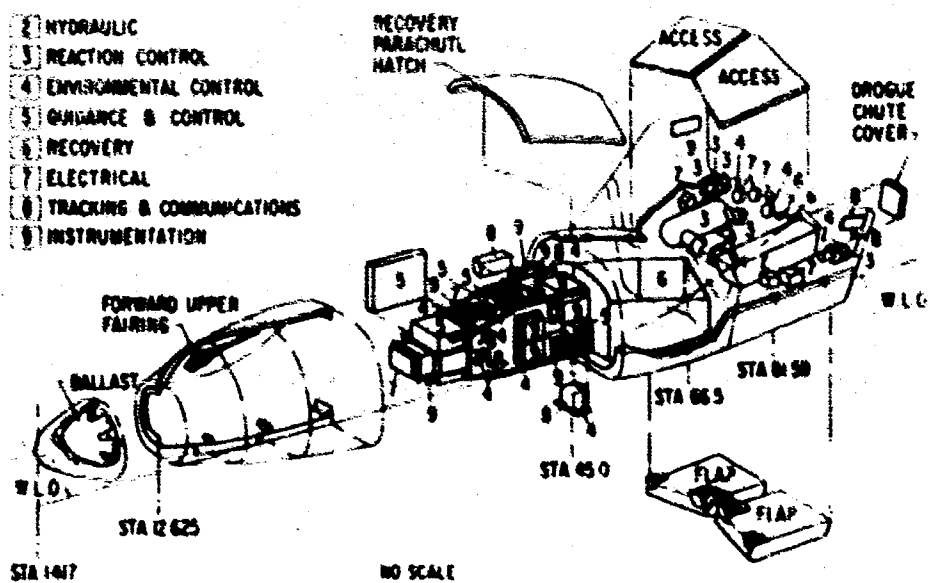


Fig. 10. Reentry Vehicle General Arrangement

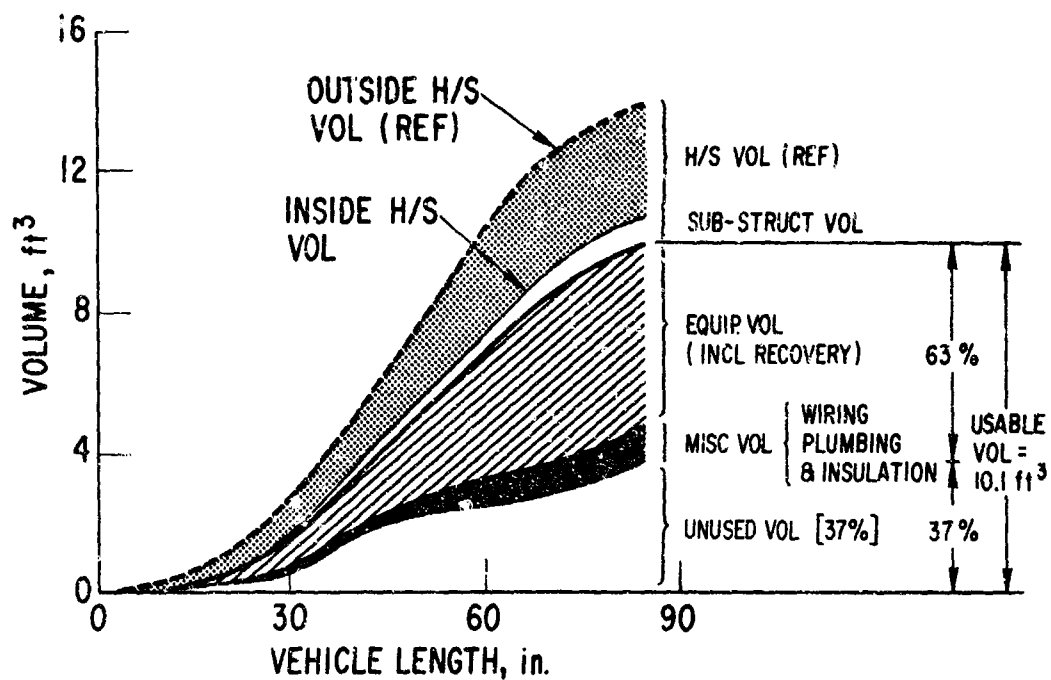


Fig. 11. Volume Utilization

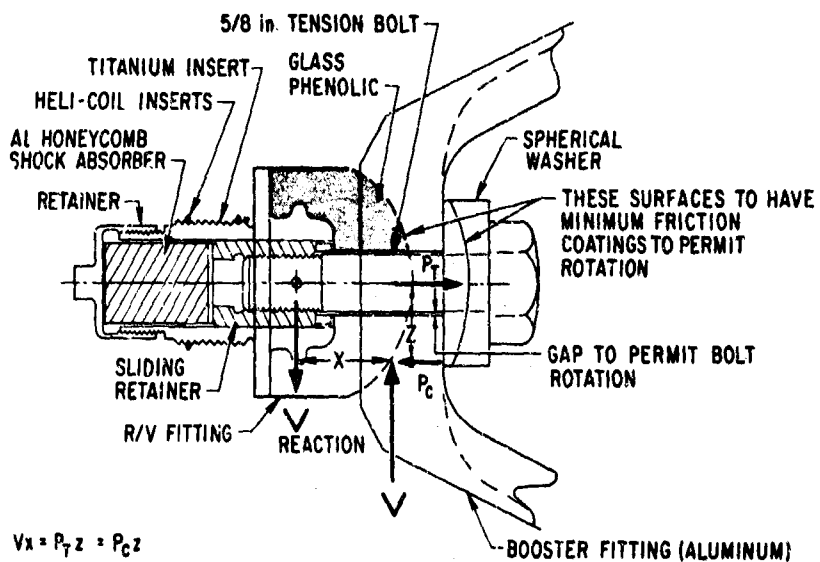


Fig. 12. Load Action of Structural Ball Joints

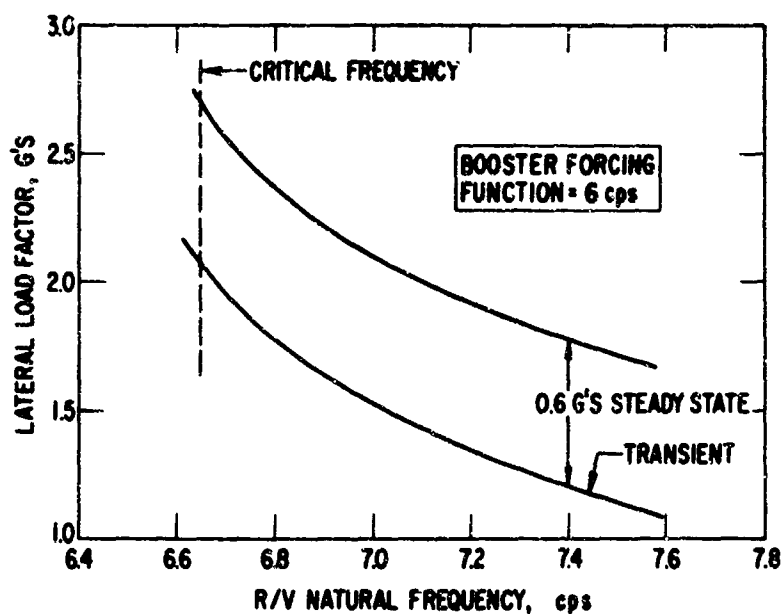


Fig. 13. Post-Launch Oscillation Condition

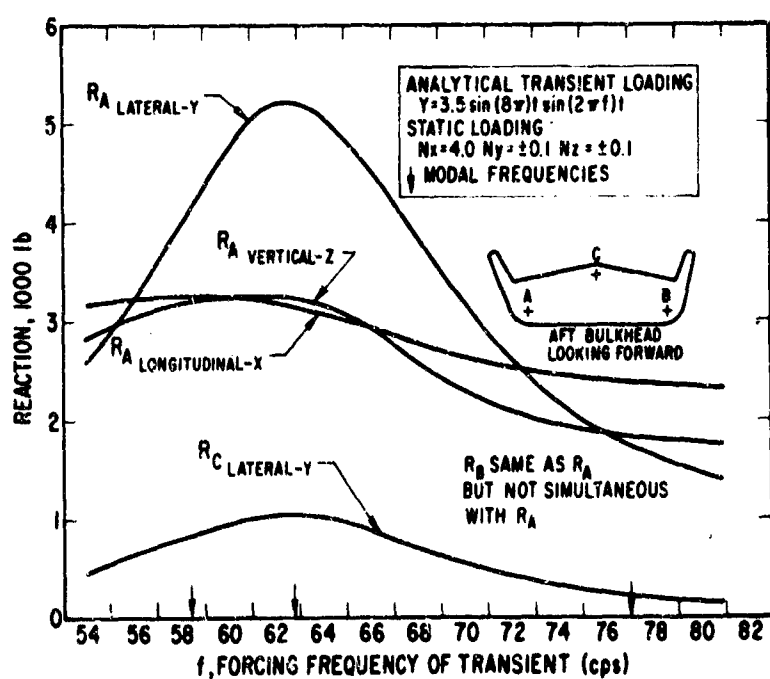


Fig. 14. BECO Transient Support Point Reactions

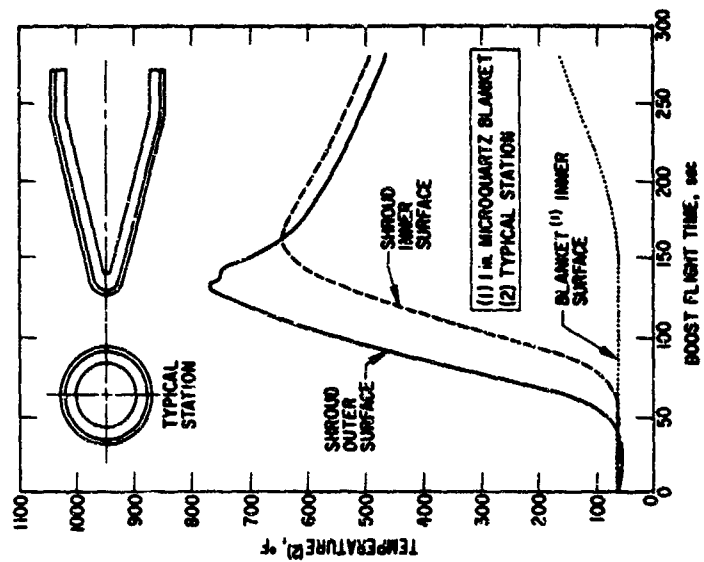


Fig. 16. Launch Firing Temperatures

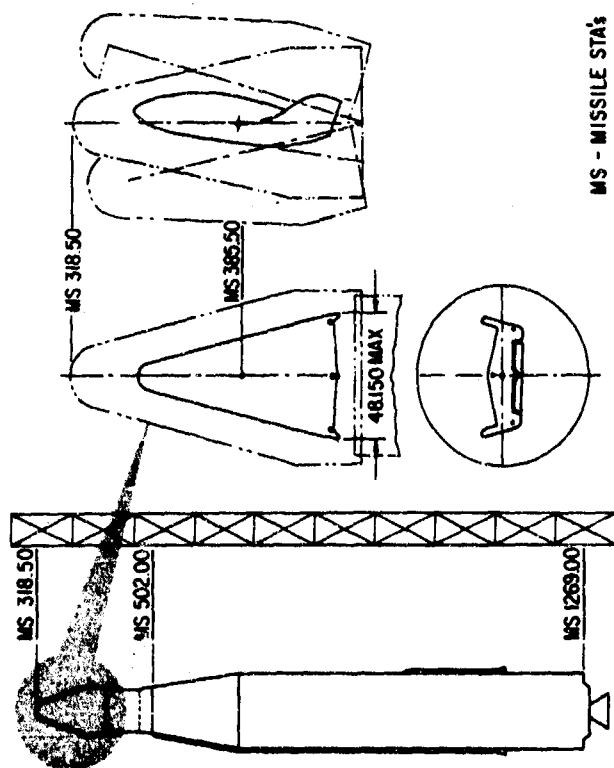


Fig. 15. Launch Firing Configuration



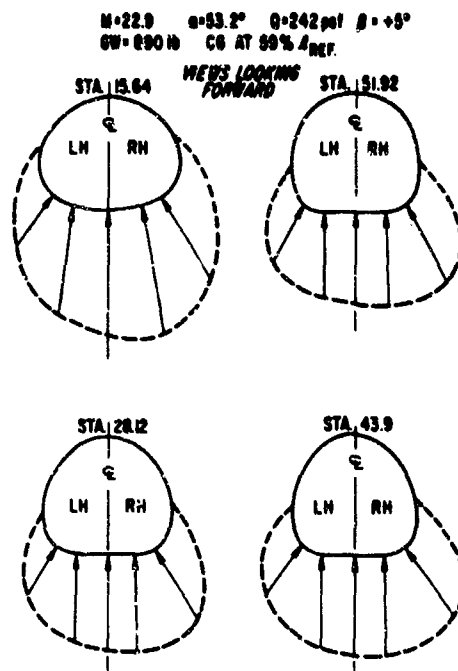


Fig. 17. Maximum Body Surface Distributions (Limit)

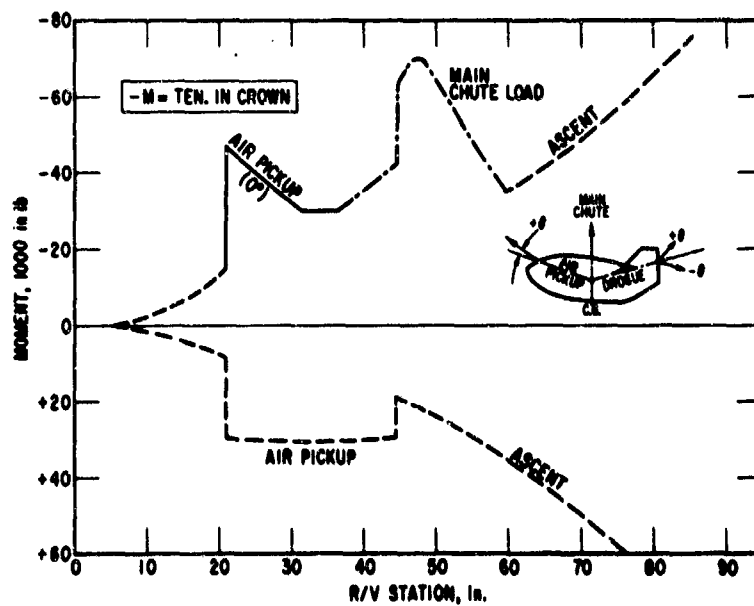


Fig. 18. Reentry Vehicle Envelope Limit Bending Moments

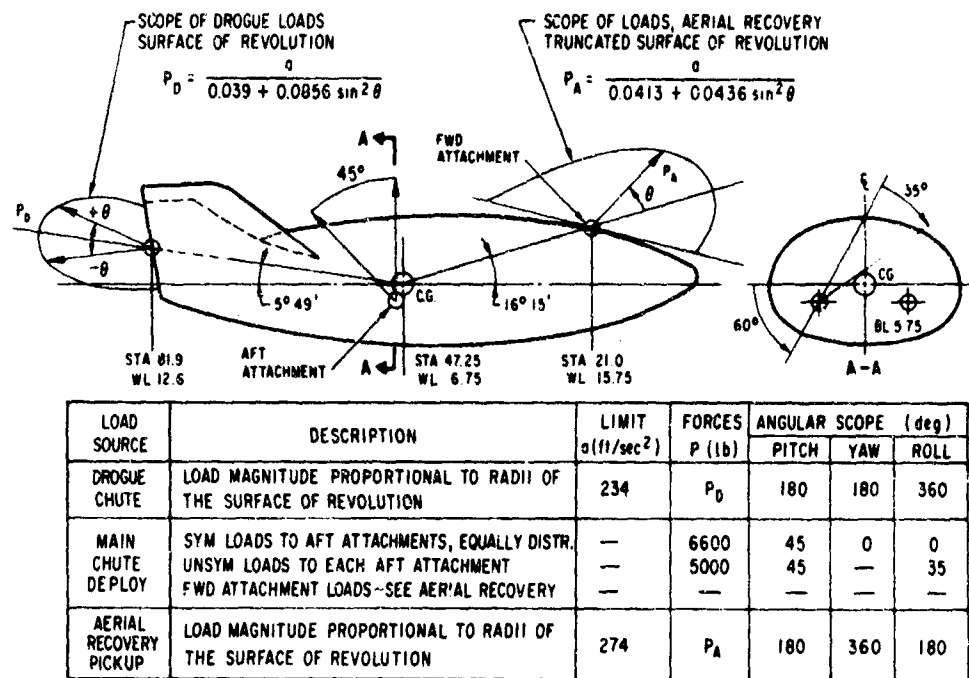


Fig. 19. Design Limit Recovery Loads (Parachute Deployment and Air Recovery Pickup)

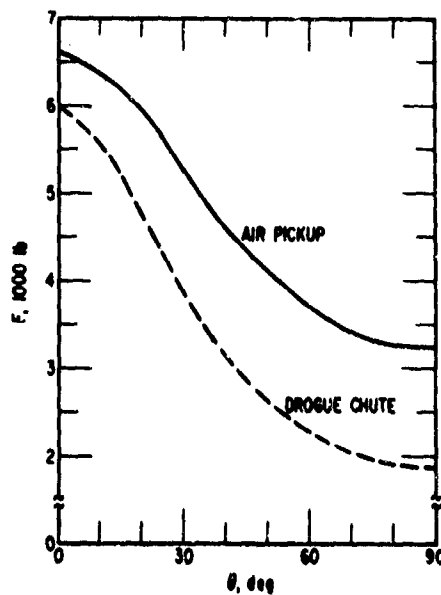


Fig. 20. Recovery Loads Application Variation

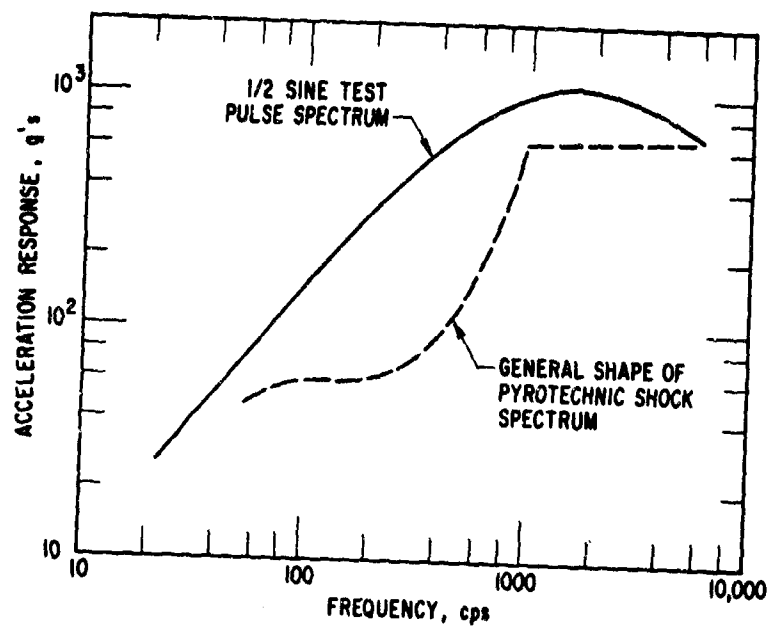


Fig. 21. Comparison of Shock Response Spectrum Shapes for Test and Actual Pyrotechnic Environment

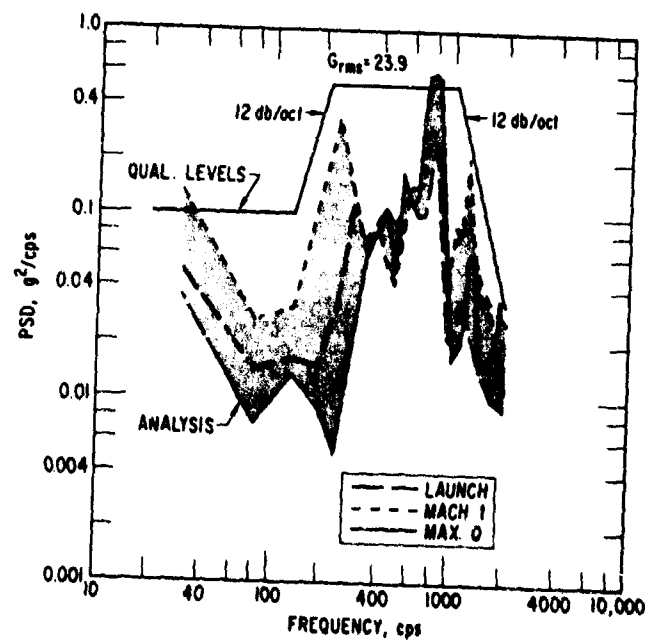


Fig. 22. 95 Percent PSD (Boost Environment)

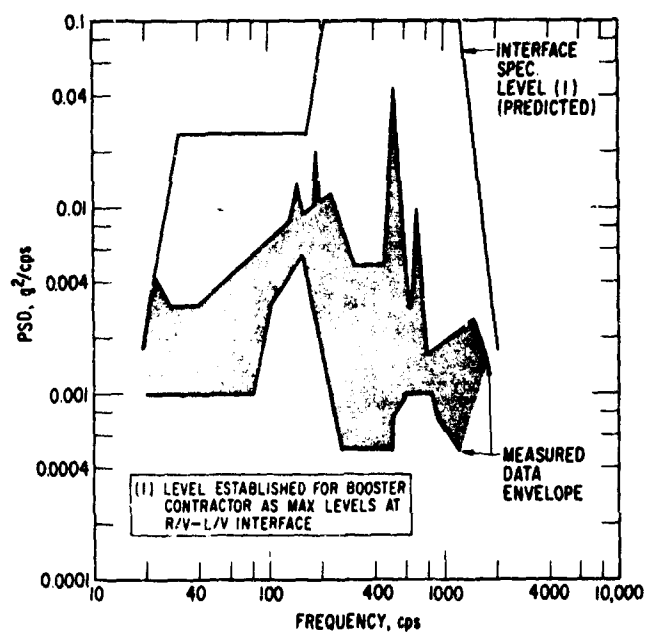


Fig. 23. Comparison of Measured Atlas Interface Vibration Data with Predicted Levels

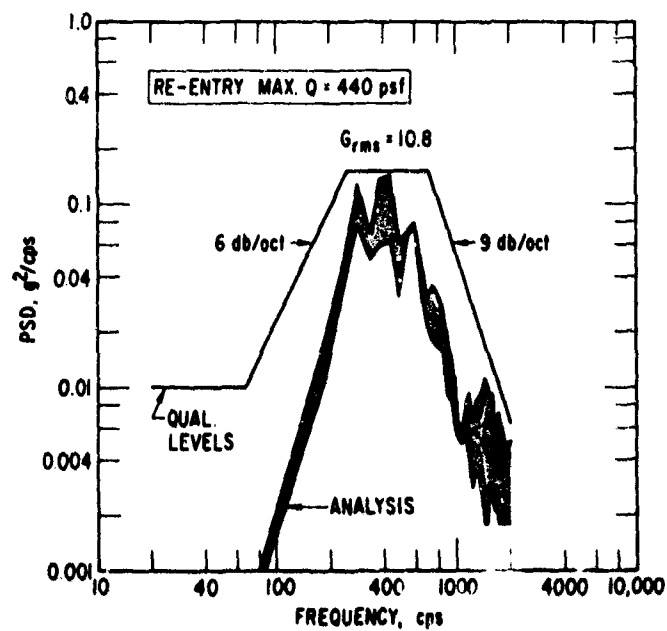


Fig. 24. 95 Percent PSD (Reentry Environment)

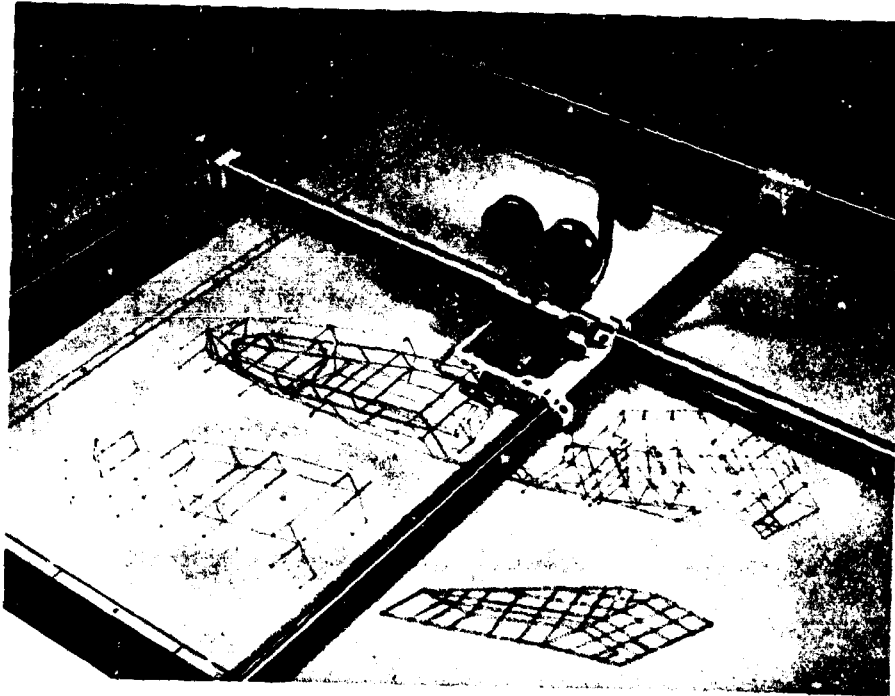


Fig. 25. Automatic Plotting Techniques

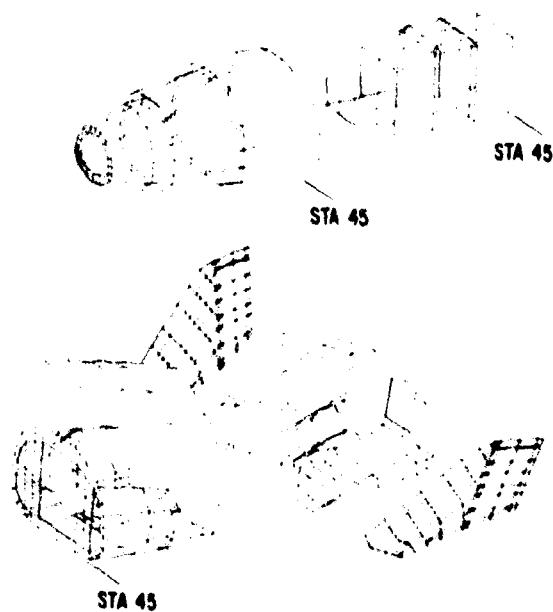


Fig. 26. Typical Trimetric Plot (Structural Model)

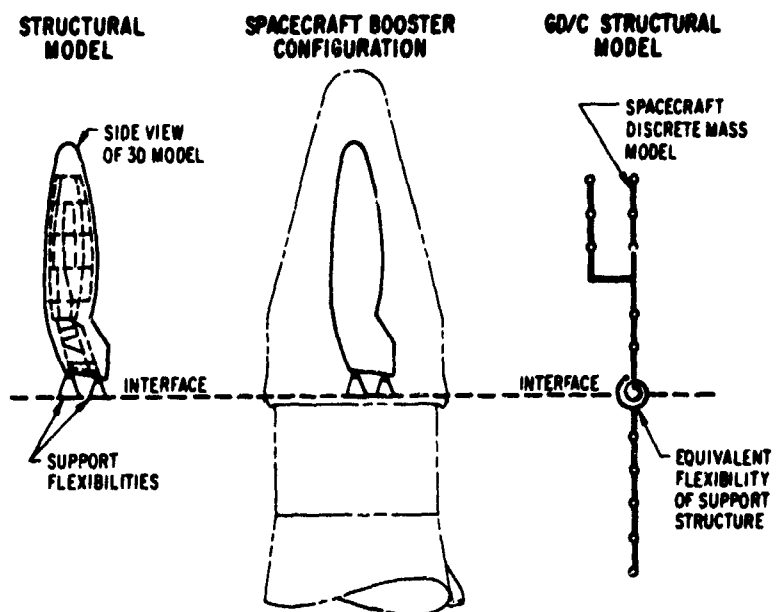


Fig. 27. Payload-Booster Interface

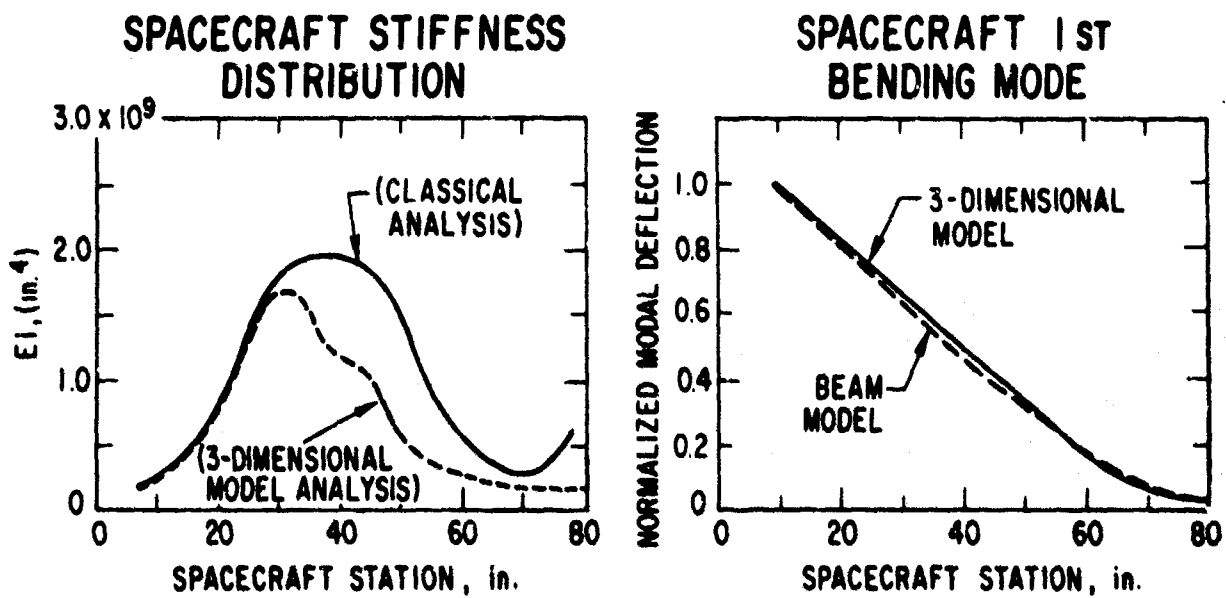


Fig. 28. Dynamic Simulation

### 3. VEHICLE HEAT SHIELD

#### 3.1 CONFIGURATION AND MATERIALS SELECTION

##### 3.1.1 Comparison of Significant Flight Parameters for Typical Reentry Systems

A comparison of the significant flight parameters for ballistic, maneuvering, reradiative, and lifting bodies indicates that lifting bodies (e.g., SV-5 (PRIME), HL-10, and M-2) encounter comparatively mild heat fluxes and shear conditions (Ref. 4) on reentry, and that except for size and velocity, the reentry environment is reasonably well simulated by many ground test facilities. The condition of low shear and high total integrated heat input for the lifting body reentry mission is compatible with the properties of low density ablative materials formulated at approximately 28 to 32 lb/ft<sup>3</sup>. Such materials have a thermal conductivity only slightly higher than still air and have adequate shear strength to resist the aerodynamic shears. Although the small PRIME unmanned vehicle has a high ratio of heat shield weight to total vehicle weight compared with ballistic reentry systems, the thermal protection system weight is more favorable when it is compared to the larger sizes compatible with manned applications. Thermal protection weights for manned SV-5 vehicles are similar to values derived from design studies for the M-2 and HL-10 configurations. These vehicles have a total weight of about 12,000 lb, and the heat shield comprises approximately 22 percent of the total vehicle weight. Although these percentages are significantly higher than for ballistic systems, the weights of the thermal protection systems for the refractory metal reradiative and the low density ablator systems are equal within the limits of accuracy of present engineering estimates.

Design studies have demonstrated that weight penalties are associated with cross range performance by any technique of vehicle configuration selected, compared to in-line reentries.

Before arriving at the current simple PRIME heat shield fabrication concept, many alternate combinations of materials and manufacturing processes were considered. An epoxy-based material similar in density and other properties to the present ESA-3560HF was developed first, and it was found to be too rigid to meet the -100°F cold soak environment.

It is believed that the thermal protection system selected for the PRIME vehicle represents the simplest and safest method to obtain, by flight tests, the basic aerodynamic, materials, and other technical data pertinent to the field of lifting reentry vehicles. Additionally, the program may obtain design data and configuration characteristic information pertinent to future manned lifting reentry vehicles.

Similarities and differences of the thermal protection systems for several of the vehicles have been studied. One of the basic differences between lifting and ballistic systems is that the latter has a minimal cold soak problem and is usually bonded directly to the substructure or to an elastomeric or foam material which accommodates differential thermal expansions. In contrast, the elastomeric PRIME material has sufficient compliance to accommodate not only the cold soak requirement for the orbital environment but also the differential thermal strains during reentry. Accordingly, the PRIME heat shield is bonded directly to the substructure, a feature which gives considerable manufacturing convenience. The Gemini and Apollo heat shields are, in many respects, similar to the SV-5 thermal protection system in that an adhesively-bonded, filled honeycomb is the primary thermal protection system. However, Gemini and Apollo have, in addition, an insulating unfilled honeycomb which is in turn adhesively-bonded to a metal supporting frame and bolted to the vehicle pressure shell and substructure.

### 3.1.2 Summary of Reentry Environment, Materials Selections, and Program Objectives

Stagnation heating as a function of reentry time was studied for several classes of R/Vs. The data indicated a similarity in the heating and the thermal



protection system requirements for HL-10, M-2, Apollo, and the SV-5. Peak shears encountered during the Apollo reentry are similar, although they occur at different body locations. The maximum shear for the PRIME vehicle is estimated not to exceed 5 psf at the sonic point and approximately 15 psf in the region of the flap where the separated flow impinges. Thus, because of the low shears, it is possible to use low density ablators over most of the R/V surface for lifting reentry.

On the basis of the foregoing technological and systems considerations, a basic program has been developed that includes: (1) suborbital demonstration of the SV-5 lifting body; and (2) a technology-oriented instrumentation of the heat shield.

Supplementing the immediate systems objectives, the vehicle could provide a test bed for new subsystems associated with lifting reentry, synergetic maneuvering demonstration, and the development of reusability-refurbishment methods and materials. Additionally, there could be an opportunity to measure control surface effectiveness in the presence of boundary layer injection of ablation products and to conduct stability margin experiments.

### 3.1.3 PRIME Flight Test Plan and Reentry Environment

Four flights are planned for the PRIME test program. The first is a minimum risk, nominal heat, straight flight; the second is a nominal cross range flight. The third and fourth flights are maximum cross range and are the most critical for the heat shield design.

A sample of the laminar heating rates and shears over the vehicle is shown in Figs. 29 and 30. The distributions show that for the majority of the surface area, the heating rates and pressures are considerably below the stagnation conditions. Typical time histories of heating rate, pressure, and shear force (see Fig. 32) are utilized over the entire vehicle surface to calculate heat shield thicknesses and structure temperatures using the Martin Company's charring ablator computer program (T-CAP).

### 3.2 ABLATION MATERIALS SELECTION

The ablative heat shield materials selected for the PRIME vehicle are the Martin Company's ESA-3560HF for the body and fins, ESA-5500 for the fin and body leading edges, and molded carbon-phenolic for the nose cap and flaps. The material selections are based on: (1) ablation performance for the PRIME reentry environment; (2) mechanical properties, particularly with respect to alleviating thermal strains; and (3) the ease of fabricating the double-contoured, varying thickness heat shield.

#### 3.2.1 Nose Cap and Flap Materials Testing and Selection

The low density ablators are not suitable for the nose cap and flap because they are high heating rate areas; a low surface recession material is required. This requirement is dictated by limits on volume, space, and shape change, and by the desire that the PRIME vehicle be an accurately-scaled version of a manned-size SV-5 lifting body. The latter requirement established fin and flap thicknesses that were incompatible with the use of ESA-3560HF with 400°F aluminum substructure. However, body lines could be maintained with 800°F fin and flap backface temperatures and appropriate design and materials changes as discussed later.

Prior to selecting the materials for the nose cap and flaps, various types of silica-, graphite-, and carbon-phenolics were evaluated for this application (Ref. 2). For the evaluation, plasma arc tests were conducted by the Martin Company and by Welsh and Slaughter (Ref. 5) at heating rates from 20 to 680 Btu/sq ft/sec for times of 300 to 1800 sec and integrated heat fluxes in the range of 50,000 to 180,000 Btu/sq ft. The plasma tests were conducted on a variety of materials in several configurations and sizes of random mold-1 and oriented specimens to develop preliminary information as to the best choice of filler, polymer, fiber and fabric orientation, and manufacturing process for the nose cap and flap component parts. Because of an aerodynamic requirement for approximately ten pressure ports closely spaced in the stagnation region, phenolic-silica was eliminated to remove the possibility that molten silica would plug the pressure ports.

In the initial phase of the material selection, monolithic two-layer molded parts with phenolic-graphite over phenolic-refrasil were considered. This approach was abandoned in favor of monolithic molded parts of random fiber carbon-phenolic, since analysis indicated approximately the same thermal efficiencies for carbon-phenolic as for phenolic-graphite over phenolic-refrasil. This approach alleviates the stress problem resulting from differential thermal expansions and differential char behavior of the two-layer system.

In the plasma tests it was observed that below about 150 to 200 Btu/sq ft/sec heat flux, the recession characteristics of all the carbon-phenolic materials tested were not markedly different from one another (i. e., recessions were within 40 percent of the mean value with the exception that  $ZrO_2$  filled material showed zero recession below about 200 Btu/sq ft/sec). However, above 200 Btu/sq ft/sec heat flux, carbon-phenolic materials with oxidation resistant fillers showed higher recession rates than the same material without filler. Presumably, this effect is due to the reaction rate controlled production of gaseous suboxides (such as SiO and ZrO) as compared to the diffusion controlled oxidation and recession of the more dense carbon char layer of straight carbon-phenolics. The data also showed that the lowest over-all recessions for the PRIME trajectories could be obtained with either carbon-phenolic or graphite-phenolic, and that fiber orientation (e. g., random, 0, and 20 deg) had little effect on surface recessions. Plasma tests demonstrated conclusively (Ref. 6) that the low thermal conductivity carbon fibers in the form of random molded test specimens do not show a more favorable (i. e., lower) backface temperature-time response than the molded FM-5065 random fiber material. The precise reason for this lack of thermal performance improvement by the substitution of low conductivity fibers in a random molding should be determined. While certain oriented low-carbon-phenolic fabric laminates developed under other Air Force sponsored research programs have shown improved thermal performance and lower thermal conductivities compared with 99 percent carbon fiber (for example, H. I. Thompson CCA-1 Carbon Fabric), no significant difference was observed

in the thermal conductivities of random fiber moldings made from the available carbon yarns and macerated fabrics when they were molded in an identical manner. Rather than continuing a search for better carbon fibers, effort was concentrated on improving the performance of the molded parts by varying the resin and the process conditions to achieve optimum thermostructural performance.

Some of the 0-deg laminates tested (Ref. 5) showed significantly lower back-face time-temperature response compared with the random fiber and 20-deg laminates. The plasma arc results could be interpreted to indicate that the 0-deg laminates showed the lowest effective diffusivity in the range of 1 to  $3 \times 10^{-4}$  sq ft/sec compared with values in the range 3 to  $4 \times 10^{-4}$  sq ft/sec for random fiber material and values of approximately  $6 \times 10^{-4}$  sq ft/sec for the 20-deg laminates. Outstanding among the 0-deg laminates was a material formulated from magnesium hydroxide fiber paper.

A further conclusion from the tests was that the laminates have a tendency to delaminate at the long test times and thick char conditions corresponding to lifting reentry. Fabric laminates tested with the fabric normal to the direction of the plasma flow delaminated in every case, whereas those laminates with the fabric planes oriented 20 deg to the axis of the plasma flow displayed a tendency to delaminate only after a deep char had developed. In all plasma tests, the molded random fiber carbon-phenolic materials remained intact. Recent tests on full-scale molded nose caps have verified structural integrity when a 10-g load was applied to the nose cap at the termination of a hot gas thermostructural test.

In summary, molded carbon-phenolic parts were selected for the nose cap and flap thermal protection materials for the following reasons:

- a. Random fiber moldings showed the same recession rate as oriented fabric composites.
- b. Molded parts showed better thermostructural integrity (no delamination) in small scale plasma tests. (This is an absolute requirement for the unsupported nose cap.)

- c. Random fiber materials have lower thermal conductivities and lower effective diffusivities than oriented (20-deg) laminates.
- d. Carbon-phenolic has lower thermal conductivity than similar graphite-phenolic materials.
- e. The low shear environment does not require oriented fabric construction.
- f. No melt layer forms to obstruct pressure ports or cause downstream erosion.

### 3.2.2 Body Heat Shield Materials Testing and Evaluation

The heat balance shown in Fig. 31 for a typical plasma test on a low density elastomeric ablator shows the low net heat input into the material and substructure under typical flight conditions and indicates that these materials are primarily a convenient-to-manufacture combination of a reradiative-insulative system for the moderate heat fluxes encountered in lifting reentry. The lower heat fluxes encountered on upper and aft surfaces could be accommodated by reradiative systems. For example, coated TZM molybdenum can be used to 42.5, coated D-6 columbium to 35.8, and Rene' 41 to 11 Btu/sq ft/sec. However, for processing, structural design, and manufacturing simplicity, the PRIME vehicle is all-ablative with a 400°F maximum aluminum substructure temperature allowed.

The efficiency of the low density materials in relation to conventional high density ablative materials is shown in Fig. 32 where integrated total heat is plotted versus thermal protection required for phenolic refrasil, phenolic-nylon, and the low density ablators such as the PRIME ESA-3560HF and the Apollo Avcoat 5026-39 material. In view of the high total heat input for the long reentry time associated with lifting reentry, the low density ablators are obviously lighter weight and make possible a reasonable ratio of heat shield to total system weight for ablative lifting bodies.

Other silicon materials applicable for use in a lifting reentry environment were evaluated by the Martin Company in plasma arc ablation tests to compare them with ESA-3560HF. These data showed that silicon materials with

higher densities were less efficient than ESA-3560HF, and that other formulations when modified and reduced to the same density were, at best, as efficient. Thus, on the basis of insulation efficiency, the ESA-3560HF is a considerable improvement over the conventional high density materials and is at least equal to the most recently developed low density materials.

The ESA-3560HF material to be used over the majority of the surface area consists of a filled elastomeric silicon reinforced with glass-phenolic honeycomb and glass fibers. This material was specially developed for the PRIME vehicle and similar lifting body configurations and, therefore, has many advantages over other ablative materials.

Most ablative materials (c.g., phenolic nylon, phenolic graphite, phenolic carbon, and phenolic refracil) have been developed for the high heating rates, high shears, and the short times characteristic of ballistic reentry and rocket nozzle environments. In these applications, surface recession rates in critical areas control, in large measure, backface temperature response. Thus, these materials are relatively dense for minimum weight loss by shear, etc., and for minimum thermochemical surface recession. However, for the low heating rate, long-time heat pulse experienced by ablating lifting bodies, insulation properties dominate materials performance. Surface recession is still influential, but its significance is much less than for the higher heating rate environments. This is especially true for silicon materials used at heat fluxes below 90 to 120 Btu/sq ft/sec. Under these conditions, very little recession occurs; therefore, new criteria are required for evaluating the performance and safety factors inherent in ablative lifting body thermal protection systems. In this new ablative application, the primary materials properties which control backface temperatures and heat shield weights are the thermal conductivity and density. These properties have been optimized for the ESA-3560HF material.

In the present state of the art, the low density ablators formulated at about 32 lb/ft<sup>3</sup> appear to represent an empirical optimum based on configuration,

fabrication, reentry environment, and system performance requirements. It is expected that, as a result of continuing Air Force and NASA development programs, further materials improvements and more efficient utilization will occur through improved thermostructural design, the development of refurbishment techniques, the development of improved fillers, and the formulation of improved lower density composites.

To evaluate the need for a backup material and to compare the ESA-3560HF material developed by the Martin Company with other commercial low density ablative materials (Ref. 2), Welsh et al. (Refs. 6 and 7) conducted screening tests in cooperation with the Air Force Materials Laboratory and Giannini Scientific Corporation at heat flux levels of 20, 60, 90, 120, and 150 Btu/sq ft/sec in a 5-in. supersonic nozzle. The specimens were flat face cylinders 2 in. in diameter and 2 in. thick. Thermal analysis was performed, based on redundant thermocouples placed at the centerline and 1 in. from the hot face. Although some initial difficulty was experienced with side and back-face heating, these problems were corrected as the test progressed, and the recession and temperature data at the 1-in. depth are considered to have provided an accurate and useful comparison of the various materials.

The materials tested were found to have insulating characteristics comparable to idealized heat conductors with thermal diffusivities between  $2$  and  $7 \times 10^{-6}$  sq ft/sec under test conditions producing no recession. As deduced from one-dimensional heat conduction analysis of the time-temperature response, a tendency was found for the apparent diffusivity to rise during some tests. For these materials, the char seemed to have a higher conductivity due to higher density or to other effects as the char layer thickened. Figure 33 illustrates the change in char density of ESA-3560HF in the zone behind the hot face. These data are believed to be typical of the changes that occur in other filled low density ablators as the char zone moves through the virgin material. The density increase at the hot face shows how pyrolytic deposition and sintering at the hot face increase density in a manner which can affect other properties.

Surface recessions of low density materials, as shown by Welsh and Slaughter (Ref. 6) in Fig. 34 for the low density ablators tested, indicate comparable recession rates at a given heat flux under this range of test conditions, with the exception that the silicon-based materials do not recede until the heat flux exceeds about 90 Btu/sq ft/sec. The charring ablator type materials showed lower recessions above the 90 to 120 Btu/sq ft/sec heat flux range.

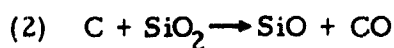
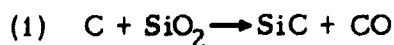
Based on thermal performance, insulation efficiency, recession characteristics, manufacturing simplicity, materials availability, and process and quality control considerations, it was concluded from the plasma tests that the low density silicon elastomeric ablation materials are a good choice for the present and future mission requirements of the PRIME vehicle. It was also concluded from these tests that there are other commercially available low density ablative materials that could be used should the need arise.

The theoretical oxygen diffusion limited recession rate for a charring ablator (char density, 11 lb/cuft) is indicated in Fig. 34 and compared with ESA-3560HF. The recession rate for ESA-3560HF obviously exceeds the theoretical maximum rate for surface combustion-controlled recession. It is also apparent that the charring ablator materials are more efficient for the high heat flux, short reentry times, while the silicon elastomers are more efficient for the milder heat fluxes and longer reentry times. The data of Fig. 34 further suggest that it is possible, by judicious formulation, to obtain an optimum ratio of  $\text{SiO}_2/\text{C}$  in the char so that it might be possible to achieve low recession at low heat flux and diffusion-limited charring recession rates at high heat flux. The ESA-5500 has been formulated according to these principles, and preliminary recession data are shown in Fig. 34 for comparison with the other materials. Because of the desire to minimize leading edge recession, the ESA-5500 material has 55 lb/cu ft density.

The data in Fig. 34 indicate a need for further understanding of the ablation chemistry of silicon materials to establish the oxygen pressure and temperature



dependence of recession rate. Such studies are in progress, and although it has not yet been possible to develop specific rate constants for use in charring ablator computer programs, it can be stated that there are principally two reactions that occur:



In general, reaction (1) occurs at temperatures below about 1350 to 1400°C, and reaction (2) predominates at higher temperatures and at low oxygen pressures. Low pressure plasma tests and laboratory studies are in progress to identify the reaction products and to determine the effect of oxygen pressure on recession rate. Depending on the ratio C/SiO<sub>2</sub> in the char, recession performance of elastomers is very different. As mentioned, advantage is taken of the high C/SiO<sub>2</sub> char ratio in the formulation of ESA-5500 material for the higher heat flux areas of the PRIME vehicle.

The composition of ESA-3560HF is such that, after charring at temperatures to 1000°C, the char is composed predominantly of SiO<sub>2</sub> and C which do not react further at an appreciable rate until a temperature of 1400°C is reached at low oxygen pressures. Chars prepared in the laboratory - by heating in argon at 600°C and then heating at low oxygen pressure at temperatures above 1400°C - sublime and leave less than 3 percent residue of the original virgin weight. Mass-loss studies of these laboratory-prepared chars carried out at a pressure of 0.033 atm and at varying oxygen partial pressures over a temperature range from 1300 to 1550°C have shown that a 1 percent oxygen partial pressure is required to suppress the ablation which at present is assumed to take place via reaction (2).

An apparent activation energy of 113 kcal/mole has been obtained for this reaction from the rates of CO formation. The rate of reaction (2) becomes

appreciable as evidenced by the destruction of platinum furnace parts due to the reaction between platinum and gaseous silicon monoxide.

The thermochemical behavior of the silicon chars in the plasma tests (Refs. 6 and 7) and in the laboratory experiments is consistent with the thermodynamic data for reaction (2) reported by Schick (Ref. 8) and Brewer and Edwards (Ref. 9) and the kinetic data reported by Rosensweig and Beecher (Ref. 10) and Blumenthal, Santy, and Burns (Ref. 11).

The pronounced increase in insulation efficiency resulting from the addition of fibers to elastomeric ablators, as reported by Clark (Ref. 12) and shown in Fig. 35, was investigated (Ref. 6) for the ESA-3560 HF material formulated at 32 lb/ft<sup>3</sup>. However, instead of the expected increase, a slight decrease in the insulation efficiency was observed. Possibly the failure to observe any large change was due to an oxygen pressure effect, an overriding effect of density on ablation performance, or differences in test conditions. In contrast to the 32 lb/ft<sup>3</sup> for the silicon materials tested in this program, the data reported by Clark were determined for materials having a nominal density of approximately 45 lb/ft<sup>3</sup> and formulated with quite different percentages of fillers. Also, the tests reported by Welsh, et al. (Refs. 6 and 7) were carried out in a low pressure (< 0.1 atm) supersonic plasma as compared with the 1 to 2 atm subsonic plasma used by Clark.

Equilibrium data (Ref. 8) for reaction (2) indicate that the dissociation pressure exceeds the plasma test pressures as reported by Welsh, et al. at temperatures above about 1400°C (radiation equilibrium heat flux 39 Btu/sq ft/sec) at pressures below 0.1 atm. As noted earlier, the elastomeric materials showed a significant recession at low pressures only at heat fluxes greater than 60 Btu/sq ft/sec corresponding to 1600°C radiation equilibrium temperature. Similarly, under Clark's (Ref. 6) test conditions (assumed 1 atm), the equilibrium dissociation pressure would exceed the test pressure at approximately 1600°C; this is 300°C lower than the calculated radiation equilibrium temperature, 1900°C, corresponding to the peak at 100 to 125

Btu/sq ft/sec heat flux displayed in Clark's data (see Fig. 35). Thus, it would appear that reaction rates, mass transport, and observed temperature corrections cause the observed elastomeric char thermochemical behavior to lag equilibrium predictions by 200 to 300°C. Additional analysis is needed to clarify the interpretation of data; however, it does appear that thermochemical effects are significant and, together with mass transfer effects, may be dominant in the optimal performance demonstrated by the data in Fig. 35.

Fibers are added to the ESA-3560HF material, but the addition is justified on the basis of the increased structural stability of the char layer, as shown typically by the comparison photographs in Fig. 36 for plasma specimens with and without 4 percent E-glass fibers. With the fiber addition, a measurable improvement in char structure and tensile strength is achieved across the interface with the virgin material. The density of the char at this interface is approximately 10 lb/ft<sup>3</sup> as shown in Fig. 33, and the char is particularly weak and fragile. The addition of fibers to reinforce the char zone does not measurably increase the thermal protection weight nor decrease thermal performance.

Although it is not possible to define precisely the effect of aerodynamic shear on the integrity and performance of low density materials at this time, tests indicate that the effect of shear is negligible for the expected flight environment. Further quantitative tests are in progress.

### 3.2.3 Mechanical Properties of ESA-3560HF

It has been demonstrated by analysis and cold soak tests that the ESA-3560HF material has sufficient low temperature elongation to satisfy the -100°F mission requirement for orbital environments. Figure 37 gives the ultimate strain versus temperature for some typical ablators compared with ESA-3560HF. Since thermal strain accounts for the major portion of the strain design problem, it is convenient to compare a biaxial thermal strain parameter versus temperature for the materials shown in Fig. 38. These

curves give the ratio of the biaxial strain to the ultimate strain versus temperature for an aluminum substructure. It can be seen that ESA-3560HF can be bonded directly to an aluminum substructure and soaked to at least -100°F without materially increasing thermal stresses in either the heat shield or substructure.

### 3.3 THERMAL/STRUCTURAL DESIGN

#### 3.3.1 Heat Shield Design Factors

The criterion that the heat shield be retained through the recovery phase is significant in that structure temperatures continue to rise for up to 300 sec after the reentry heat pulse because of the soak-out of the heat in the hot heat shield. Therefore, the temperature rise after parachute deployment is essential in establishing the heat shield thicknesses and in structural analysis of the recovery phase, particularly air pickup. This stems from the requirement that the flight tests provide for recovery of the heat shield for post-flight evaluation. Since it is most probable that the heat shield would be retained in manned applications, this criterion is not peculiar to the test flights. The method of combining thermostructural loads is summarized in Section 2.3.4.

The heat shield-structure bond and the heat shield strain safety factors are unique to the heat shield. A safety factor of two on the bond was established on the basis of the relatively high temperature to which the bond is exposed (up to 800°F). A safety factor of two on the heat shield strain was established to account for tolerances in material properties and structure deflections.

A study was conducted to define the magnitude of the safety factors and to determine how these factors, singly and in combination, should be applied to the heat shield thickness. Since the function of the heat shield is to protect the structure to a prescribed temperature limit, the factors which influence the ability of the heat shield to meet this temperature limit are: (1) unexpected and normal variations in the reentry environment and the accuracy with which one can predict this environment; and (2) the heat shield thermal performance

and the ability to predict this performance from plasma tests. It is assumed that the reentry environment and its prediction can be combined into a tolerance on heat input, and that variations in heat shield performance and analysis can be combined into a factor on heat shield thickness. The heat shield design thickness safety factors derived from this study are summarized in Table 5.

An evaluation was conducted of heating rate analyses and wind tunnel test data to determine the expected accuracy of the calculated heating rates. This was divided into the precision of predicting the stagnation heating rate ( $q_{stag}$ ) and the precision of predicting the ratio of the local heat flux ( $q_{local}/q_{stag}$ ) at a given location. These errors were then combined into a safety factor on heat input.

A similar evaluation was made for heat shield performance derived from plasma arc test data and the analytical correlations with the design properties. The resulting factor was applied to the heat shield thickness to account for tolerances in the heat shield performance and analysis.

In practice, these two factors are used by applying the heat input factor  $F_q$  to the design trajectory heating rate and calculating the heat shield thicknesses with the Martin Company's charring ablator computer program. The calculated thicknesses are then increased by a 10 percent thickness factor.

### 3.3.2 Nose Cap Construction Details and Testing

The self-supporting nose cap structure consists of a molded FM-5065 carbon-phenolic shell that burns and chars during reentry. Ballast is located inside the nose cap and is also bolted to the aluminum bulkhead. Figure 4 shows the nose cap configuration and ballast.

The nose cap shell is sized to limit the internal temperatures to 400°F and it ranges in thickness from 3.5 in. at the stagnation point to 1 in. at the top. The predicted surface recession ranges from zero at approximately station 12 to 0.5 in. at the stagnation point.

Table 5. Design Limit Load Factors for PRIME Vehicle

Body Lower Surface and Leading Edges:

$$F_q = 1.15 \text{ for } q/q_s \text{ values greater than } 0.007$$

$$F_q = 1.25 \text{ for } q/q_s \text{ values equal or less than } 0.007$$

Fin Leading Edge:

$$F_q = 1.15 \text{ (based on } q/q_s \text{ for yaw angle of } 2.5 \text{ deg)}$$

Fin Outboard Surface:

$$F_q = 1.25 \text{ (based on } q/q_s \text{ for yaw angle of } 2.5 \text{ deg)}$$

Lower Surface of Lower Flaps:

$$F_q = 1.12 \text{ (based on } q/q_s \text{ for flap at a deflection corresponding to flap trim deflection plus } 8 \text{ deg)}$$

All Upper Surfaces:

$$F_q = 1.5$$

Full-scale nose cap tests have been conducted in a plasma arc facility and in a hot gas facility to verify the design insofar as is possible by ground testing. The plasma arc test was conducted at the average stagnation heating rate of 175 Btu/sq ft/sec for the total reentry time of 1100 sec and a total stagnation heat input of 192,000 Btu/sq ft. The heating rate, pressure, and nozzle size had to be compromised because of plasma arc size limitations. This resulted in the decision to test with a 10-in. supersonic nozzle which did not completely simulate heating rate distributions over the aft portion of the cap. Therefore, a second series of tests was conducted in a 14-in. hot gas facility; these tests concentrated on the aft portion of the cap with the stagnation heating below the maximum level.

A particular development and ground test problem has been the verification of the integrity of the thick char zone in the stagnation region. The stagnation zone is 3.5 in. thick, and the char has a tendency to separate along a contour surface approximately 1.5 in. in from the stagnation point as shown in Fig. 39. This separation is due to stresses developed during heat-up, and the problem is still under intensive test and analysis because of the critical area involved. However, preliminary test results indicate that the nose cap is conservatively designed for the expected critical loads. For example, at the end of a hot gas test and while the specimen was still hot ( $> 400^{\circ}\text{F}$ ), the nose cap was subjected to a 10-g drop test to verify the adequacy of the attachment lugs. This test simulated the loads during air recovery, a critical design condition for the nose cap.

### 3.3.3 Body Heat Shield

The general arrangement of the body heat shield joint attachments is shown in Fig. 40. The heat shield consists of the ESA-3560HF ablative material in E-glass phenolic honeycomb bonded directly to the aluminum structure. The adhesive provides a reliable bond that can withstand higher structure temperatures than aluminum. Heat shield thicknesses are sized to limit the aluminum temperature to  $400^{\circ}\text{F}$  considering the local surface heat input. Thus, the heat shield thickness varies considerably over the body - ranging from 2.75 to 0.8 in. Typical body cross-sections and edge members are shown in Fig. 40.

At the various discontinuities in the heat shield, low density refrasil-phenolic edge members are used; access to attachment screws is provided by threaded plugs in the edge members similar to those shown in Fig. 40. The body pressure ports, as discussed subsequently, consist of ceramic tubes through the ablative layer with a metal attachment at the substructure to retain the pressure port and provide a pressure seal to the instrument tubing.

Thermal stresses in the body structure are significant and in most locations establish the thickness of the aluminum skin. Temperature gradients causing these stresses result primarily from variations in the reentry time-temperature response of the heat shield to the wide range of heating rates over the body. When the heat shield is sized to protect the structure to the design temperature, the low heating rate areas reach peak temperature before the high heating rate areas. Thus, the top of the vehicle which has a low heat input rises in temperature faster than the higher heat input area on the bottom, even though both are designed for the same peak temperature. Furthermore, because of this temperature gradient and the high conductivity of the skin, a significant amount of heat is transferred from the top to the bottom of the vehicle. This alleviates the thermal stresses but requires two-, and in some areas three-, dimensional thermal analyses.

#### 3.3.4 Fin and Antenna Window Heat Shield

To meet the aerodynamic shape requirements on thickness, the fin structure temperature was increased to 800°F compared with 400°F on the body. The adequacy of the adhesive bond at 800°F is defined by the heat shield-structure bond strength data shown in Fig. 41 and is further substantiated by the high temperature strength data reported by the manufacturer. A conservative heat shield design is used here because of the allowance of an 800°F backface maximum temperature.

The fin structure consists of brazed beryllium skin over steel honeycomb panels except for the region of the antenna window where a beryllium heat sink structure is used. The details of the fin are shown in Fig. 42. The fin heat



shield material is ESA-3560HF except for the antenna window where Teflon is used. The fin heat shield thicknesses range from 1 in. on the outboard side to 0.3 in. on the inboard side. The fin leading edges are ESA-5500 to minimize surface recession. The fillet radius between the fin and body is filled with a fiber-reinforced caulking compound of composition similar to ESA-3560HF, and the differential strain between the two structures is absorbed by the ablative material.

The antennas are Teflon-covered slots in beryllium plates at the outboard tip of each fin. The heat sink capacity of beryllium is required since the Teflon is not as efficient as the surrounding heat shield which defines the local thickness. The Teflon is attached mechanically to the beryllium by inserts in the Teflon.

#### 3.3.5 Flap Heat Shield

The flap has an 800°F structure to reduce the required heat shield thickness and requires a beryllium heat sink structure to make the body lines conform to the desired aerodynamic shape. The flap receives high heating rates, and therefore uses the molded carbon-phenolic heat shield on the lower surface to minimize surface recession. The upper surface which is exposed to much lower heat uses ESA-3560HF material. The over-all size of each flap is approximately 12 by 12 in. with the beryllium structure 0.5 in., the carbon-phenolic 1.65 in., and the ESA-3560HF 0.3 in. thick. The detail arrangement of the flap is shown in Fig. 43. A refrasil-phenolic block is bonded around the flap brackets to form the local heat shield and it rubs on a mating carbon-phenolic block mounted on the body. These blocks are slotted to receive the support brackets, and rotation is provided by machining on a radius from the hinge line. Thus, the brackets and bearings are protected from direct exposure to the local air flow. The leading edge seal is established with molded carbon-phenolic blocks mounted on the top of the flap and on the body adjacent to the flap. This block is machined to match the flap leading edge radius, and the air flow is further restricted by utilizing a 0.060-in. clearance between the two.

It is not possible to run full-scale flap tests in a plasma facility because the flap is too large. Therefore, the verification test program consists of: radiant lamp tests on the full size bare beryllium structure; plasma tests to verify the bearing assembly design; hot gas tests to verify the thermostructural integrity of the full size flap and bearing assembly; analysis of Mach 20 flap-gap heating data; and reliance on the charring ablator computer program to verify backface temperatures in critical areas. It is believed that this approach exhausts the available sources of ground verification, and only by actual flight tests can complete verification be achieved.

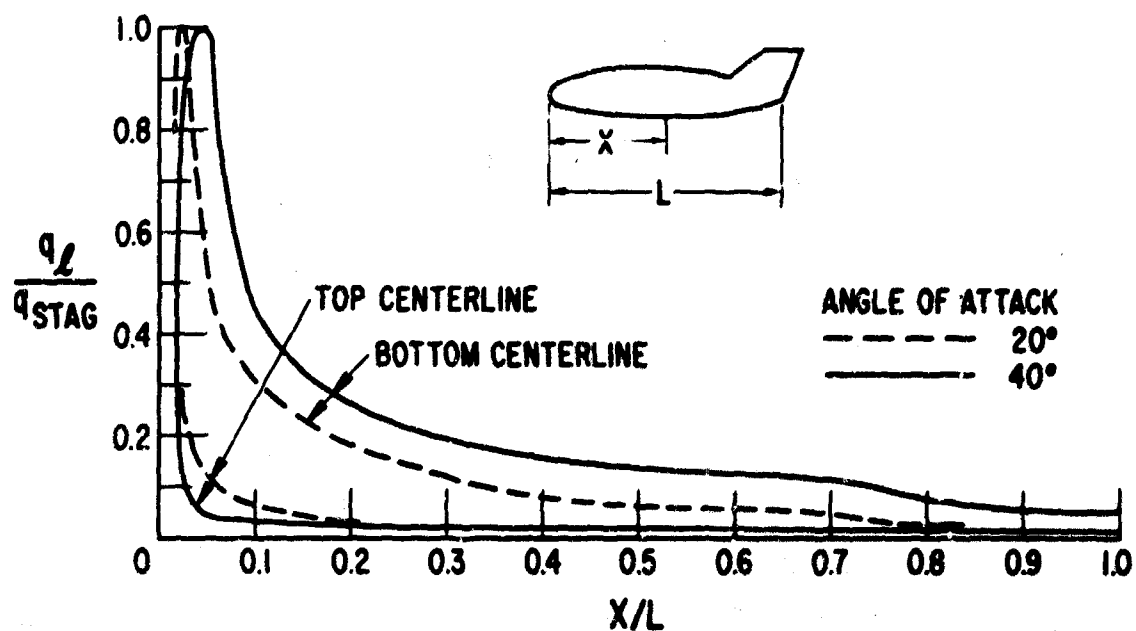


Fig. 29. Typical Local Heating Rate Ratio

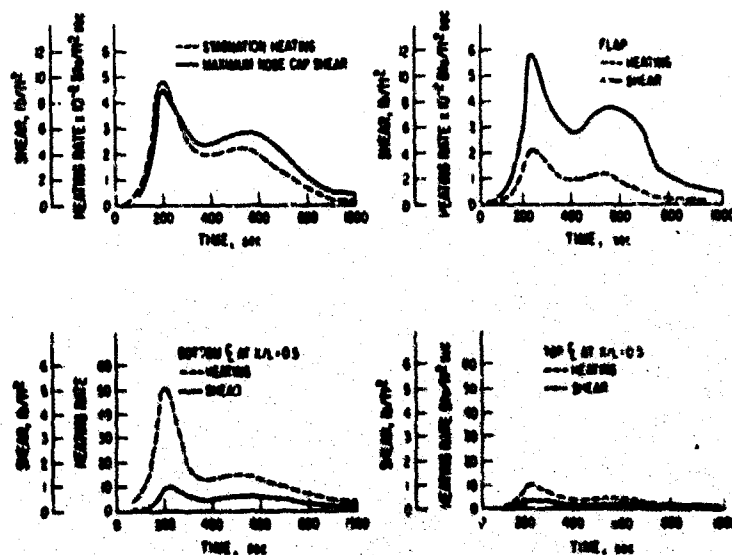


Fig. 30. Typical Shears and Heating Rates for Nose Cap, Flap, Top, and Bottom of PRIME Vehicle

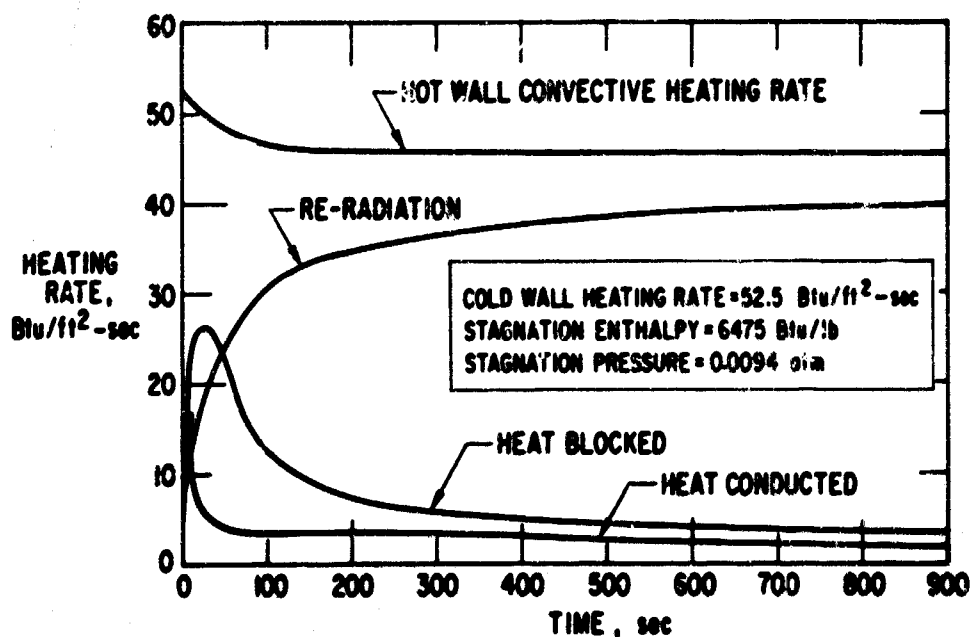


Fig. 31. Typical Heat Balance for Low Density Ablator Plasma Arc Test at Moderate Heat Flux Showing Low Net Input to Substructure

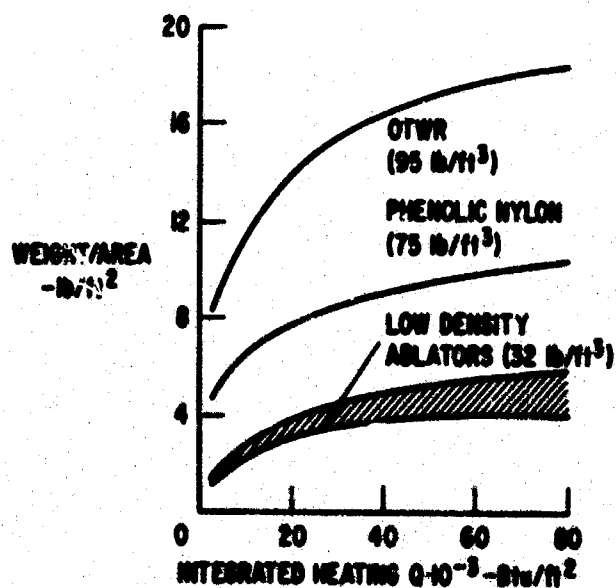


Fig. 32. Weight Comparison of Low Density Ablators with Standard Ablators for Typical Lifting Body Orbital Reentry Conditions (400°F Backface Temperature)

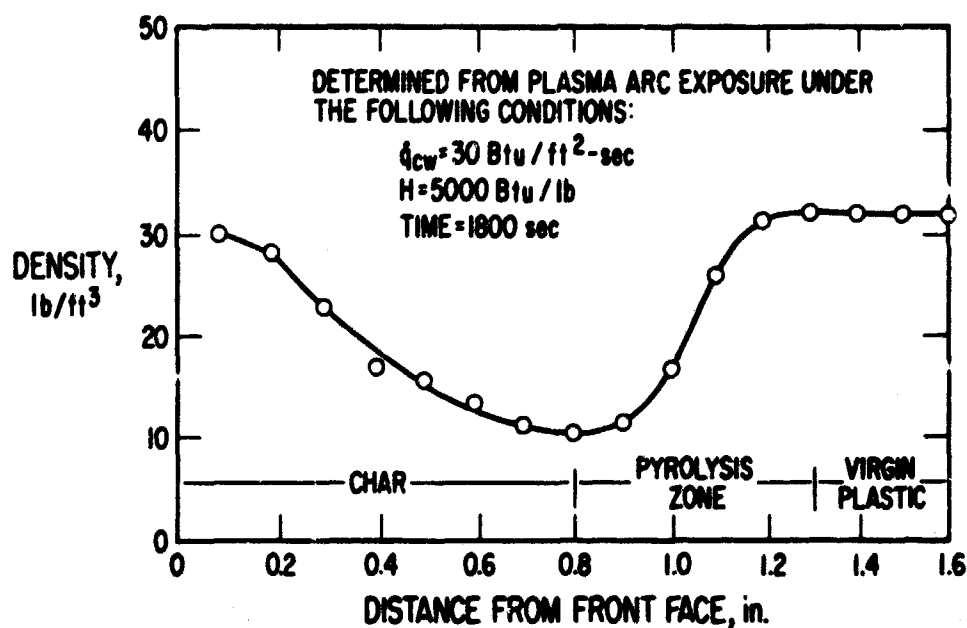


Fig. 33. Typical Density Distribution for ESA-3560H Through Char and Pyrolysis Zones

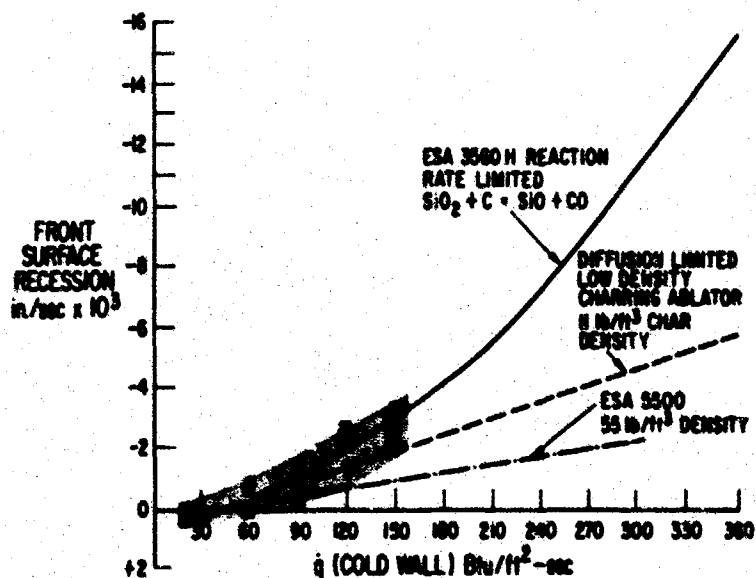


Fig. 34. Recession Characteristics of Low Density Ablators (32 lb/cu ft)

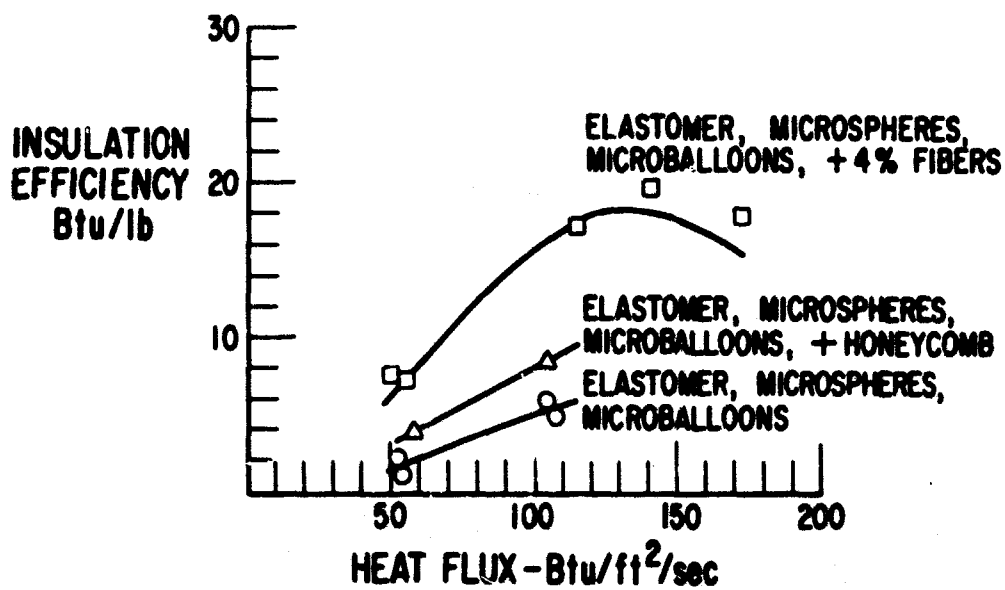


Fig. 35. Insulation Efficiency of NASA/Langley Purple Blend with Fiber Addition (from Clark, Ref. 12)



Fig. 36. Improved Char Reinforcement by Glass Fiber Addition to ESA-3560HF

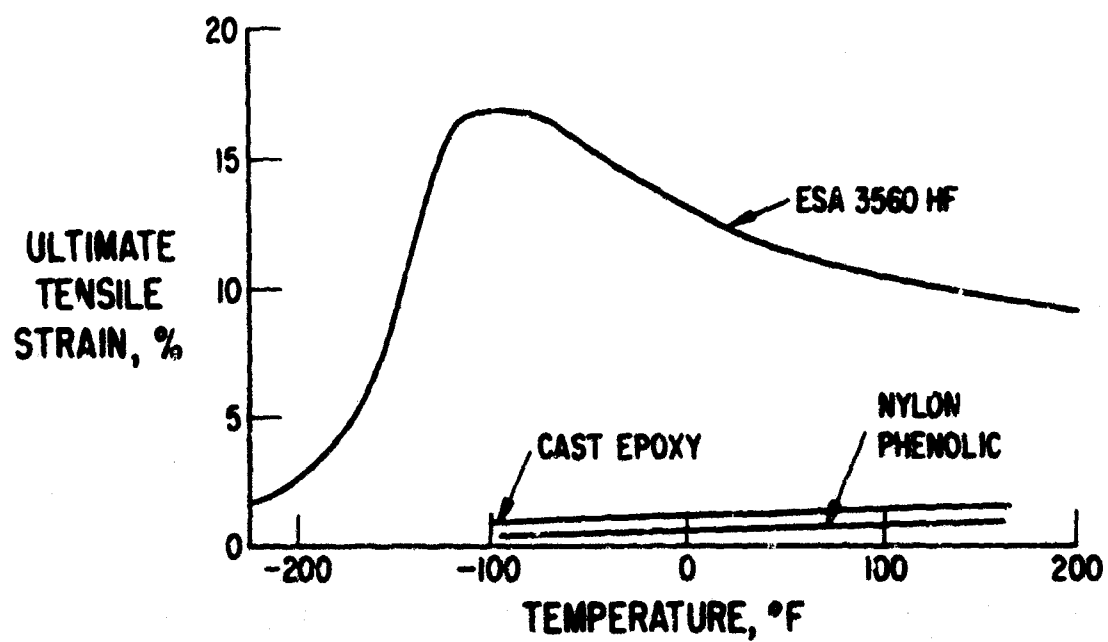


Fig. 37. Ultimate Strain for Various Materials

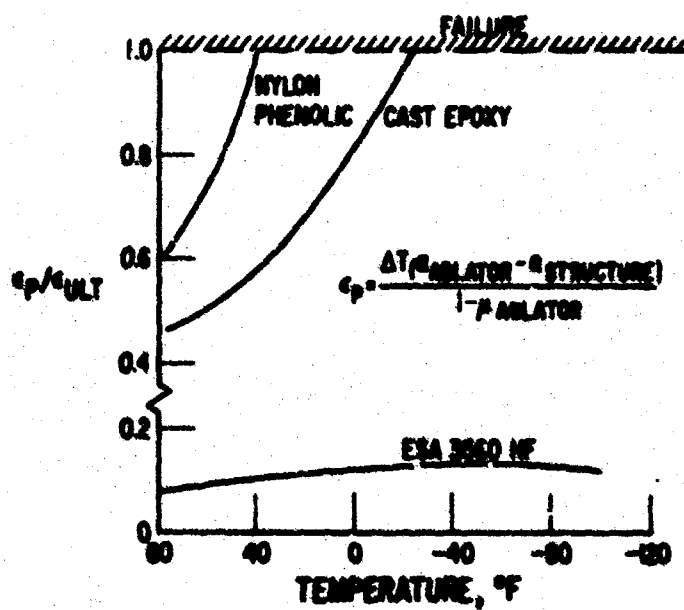


Fig. 38. Thermal Strain Failure Parameter versus Temperature



Fig. 39. Carbon-Phenolic Nose Cap After Heat Test

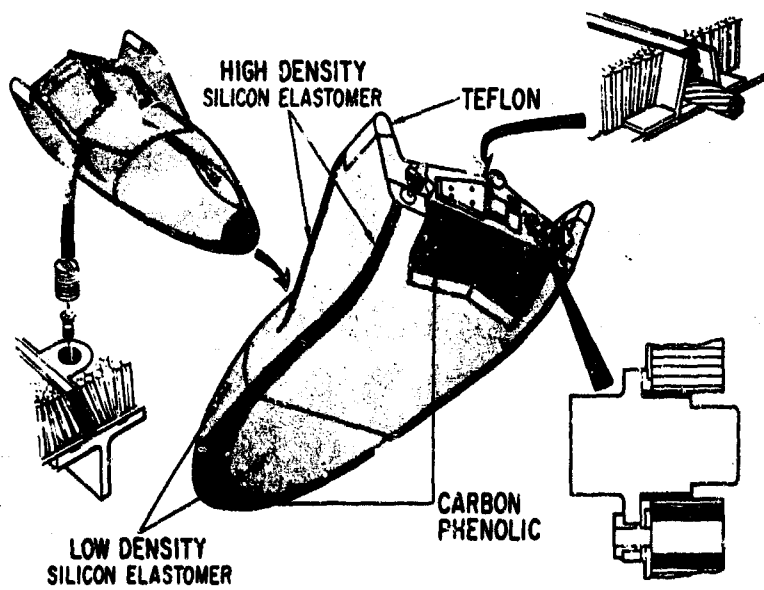


Fig. 40. Body Heat Shield Details



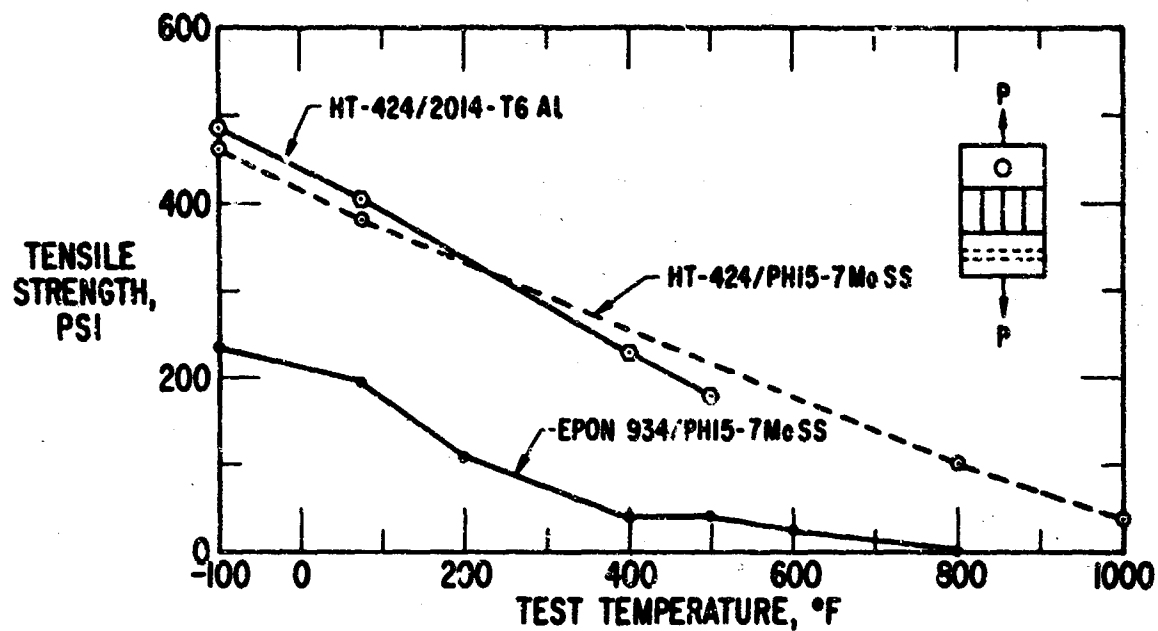


Fig. 41. Bond Strength of HT-424 and EPON 934 Adhesives for Bonding E-Glass to Stainless Steel and Aluminum

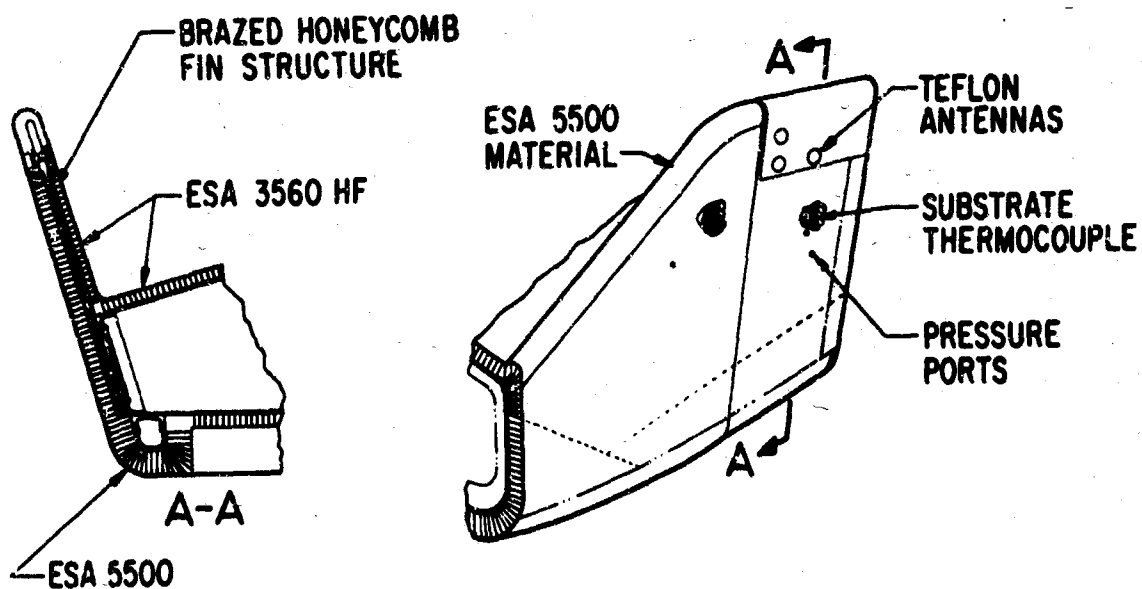


Fig. 42. Fin and Antenna Window Details

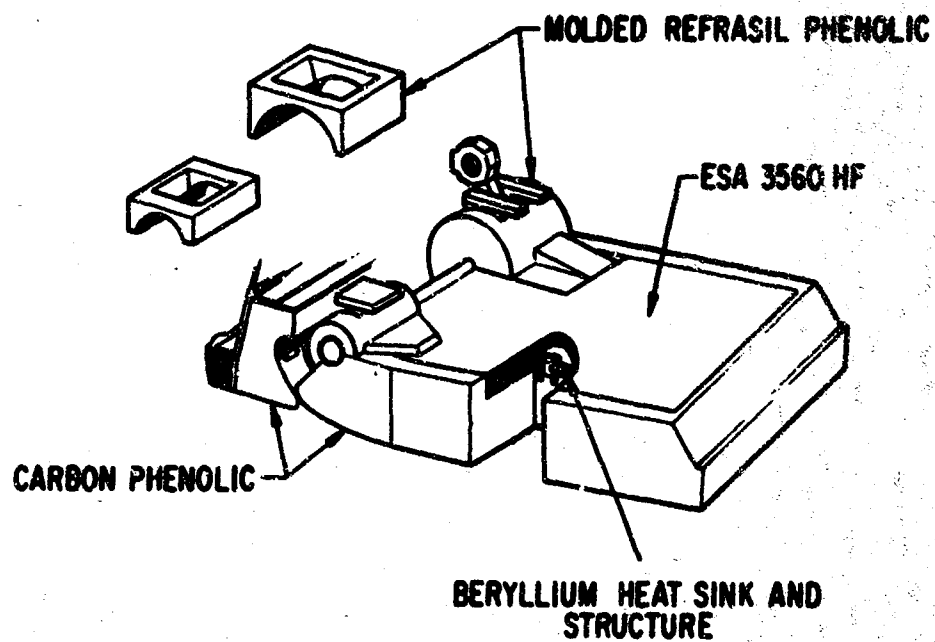


Fig. 43. Flap Heat Shield Details

## REFERENCES

1. O. B. Gates, "Project PRIME--Maneuvering Reentry Vehicle," Paper presented at Tenth Symposium on Space and Ballistic Missile Technology, San Diego, California, 4-6 August 1965.
2. J. Meltzer, J. I. Slaughter, and D. V. Sallis, "Thermal Protection System for the SV-5 (PRIME) Ablative Lifting Reentry Vehicle," Paper presented at Tenth Symposium on Space and Ballistic Missile Technology, San Diego, California, 4-6 August 1965.
3. S. Kaufman and D. B. Hall, "Static and Dynamic Analysis by a Matrix Force Method," Shock and Vibration Bulletin No. 34, Part 3, Martin Co., (December 1964).
4. A Lifting Reentry, Horizontal Landing Type Logistic Spacecraft, NASA Report X64-13943, The Boeing Company (3 February 1965) (Contract NAS9-1689).
5. W. Welsh and J. I. Slaughter, Plasma Arc Tests of Carbon-Phenolic Materials for Lifting Reentry Vehicle Applications, TDR-669(5250-40)-1, Aerospace Corporation (to be published).
6. W. Welsh, D. Leeds, K. Starner, and J. Slaughter, Low Density Ablation Materials Survey, TDR-469(5240-10)-17, Aerospace Corporation (to be published).
7. S. L. Grindle and J. P. Todd, Evaluation of Thermal Protective Systems Under Simulated Reentry Conditions, ML-TDR-64-293, Giannini Scientific Corporation (February 1965).
8. H. L. Schick, "A Thermodynamic Analysis of the High Temperature Vaporization Properties of Silica," Chemical Reviews, 60, 331-362 (August 1960).
9. L. Brewer and R. K. Edwards, "The Stability of SiO Solid and Gas," J. Am Chem Soc, 58, 351 (1954).
10. R. E. Rosensweig and N. Beecher, "Theory for the Ablation of Fiberglass-Reinforced Phenolic Resin," AIAA Journal, 1, 1802 (1963).
11. J. L. Blumenthal, M. J. Santy, and E. A. Burns, "Kinetic Studies of High Temperature Carbon-Silica Reactions in Charred Silica-Reinforced Phenolic Resins," Paper No. WSCI 65-25, Western States Section - The Combustion Institute Fall Meeting (October 1965).
12. R. Clark, Environmental Parameter Effects on Performance of Low Density Silicone-Resin and Phenolic-Nylon Ablation Materials, NASA TN-D-2543 (January 1965).